Artificial metallo-proteins for photocatalytic water splitting: stability and activity in artificial photosynthesis

Opdam, L.V.

CHAPTER 3

AN ARTIFICIAL METALLOENZYME THAT CAN OXIDIZE WATER PHOTOCATALYTICALLY:

DESIGN, SYNTHESIS, AND CHARACTERIZATION

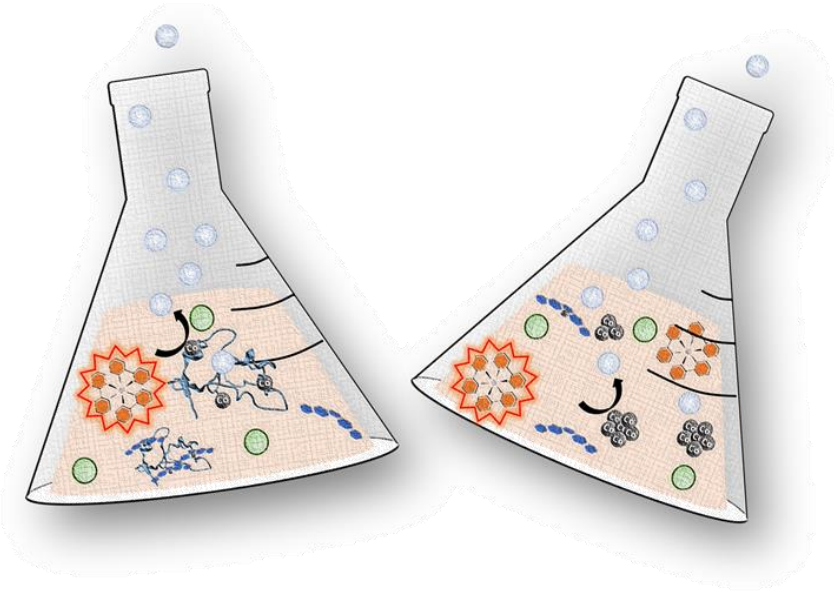

Accepted as Opdam, L[†] and Polanco, E[†]; Passerini, L; Huber, M; Bonnet, S and Pandit, A. An artificial metalloenzyme that can oxidize water photocatalytically: design, synthesis, and characterization. *Chemical science* **2024.**

†Shared first authors with equal contribution to the work

ABSTRACT

In nature, light-driven water oxidation (WO) catalysis is performed by Photosystem II *via* the delicate interplay of different cofactors positioned in the protein scaffold. Artificial systems for homogeneous photocatalytic WO are based on small molecules that often have limited stability and solubility in aqueous solutions. In this work, we explored the use of an artificial metalloprotein (ArM) to alleviate these issues. A haem-containing electron transfer protein, cytochrome b_5 (CB5) served to host a first-row transition-metal-based WO catalyst, CoSalen (Co^{II}Salen, where is H_2Salen = N,N'-bis(salicylidene)ethylenediamine), thus producing an ArM capable of driving photocatalytic WO. The CoSalen ArM formed a water-soluble pre-catalyst in presence of $[Ru(bpy)_3](ClO_4)_2$ as photosensitizer and $Na_2S_2O_8$ as sacrificial electron acceptor, with photocatalytic activity similar to that of free CoSalen. During photocatalysis the CoSalen-protein interactions were destabilized, and the protein partially unfolded. Rather than forming CoOx nanoparticles as free CoSalen does under photocatalytic WO conditions, the CB5:CoSalen ArM showed limited protein crosslinking and remained soluble. We conclude that a weak, dynamic interaction between a cobalt species and *apo*CB5 was formed, which generated a soluble, catalytically active adduct during photocatalysis. A detailed analysis was performed on protein stability and decomposition processes during the harsh reaction conditions of WO, which will serve for the future design of WO ArMs with improved activity and stability.

1 INTRODUCTION

In nature, the challenging reaction of light-driven water oxidation (WO) catalysis is performed by Photosystem II (PSII). In this system, light capture and charge separation processes are coupled with WO catalysis *via* different cofactors that are carefully positioned in a protein matrix [1,2]. As water splitting is one of the most attractive ways to achieve sustainable H_2 production as a replacement for fossil fuels, the design of artificial photocatalysts for water oxidation has generated tremendous interest during the last two decades. Researchers have managed to develop photocatalytic water oxidation systems based on small molecules or macromolecules,[3–6] but many of these compounds are based on precious

metals [7–11]. Recently, a significant variety of earth-abundant metal complexes have been proposed as more sustainable and accessible water oxidation catalysts (WOCs) [4,12–16]. Still, in homogeneous systems, the main drawback of most of these catalysts, whether based on abundant or scarce metal, is their instability and limited solubility in aqueous solutions [12,17].

In this study, we address the question of whether so-called artificial metalloproteins (ArMs) can serve to alleviate these issues. During evolution countless enzymes have developed, approximately half of which are metalloproteins [18]. The function of each enzyme is defined by the properties of its metal cofactors, which are carefully tuned by the protein environment to drive a specific chemical reaction. This tuning leads to high specificity both in terms of reactant selectivity and product formation. In addition, it makes complex chemical reactions possible under extraordinarily mild conditions [19,20]. The potential advantages that may result from the control of the 2nd coordination sphere around a metal catalyst have led to the development of very active research on ArMs [21–24]. ArMs are being developed as potential greener alternatives to different reactions such as O_2 reduction, cyclopropanation, or the Diels Alder reaction, which can be obtained in much milder conditions and aqueous solvents, compared to classical chemical synthesis [25–36]. The application of ArMs for the production of renewable energy has gained increased interest during the last decade [37–42]. Modified hydrogenases, flavodoxin, or myoglobin, have been proposed as examples of photoactive ArMs that can drive H_2 evolution under light irradiation [37,43,44]. However, examples of ArMs that can catalyse O_2 evolution are scarce [45–47]. Of the two half-reactions of water splitting, *i.e.,* water oxidation (WO) into O_2 and proton reduction into H_2 [3,48–51], the former remains the most challenging, both kinetically and thermodynamically. Moreover, the harsh conditions during the WO reaction are potentially detrimental to protein stability. Extreme redox chemistry is required in PSII to photocatalyse WO [52]. Nature did not find a solution to prevent protein damage during this reaction and in plants, for example, protein units at the active site of PSII are replaced about every hour [53].

In Chapter 2 the interaction between three types of haem proteins and small-molecule water oxidation catalysts based on tetradentate ligands coordinated to ruthenium or cobalt was investigated. This study was aimed

at selecting a protein-WOC couple that would strongly bind the WOC in conditions compatible with protein stability. The study led to the selection of a couple comprising cytochrome b_5 (CB5), an electron-transfer protein, and the earth-abundant WOC [Co^{II}Salen] (CoSalen), where H_2Salen = N,N'-bis(salicylidene)ethylenediamine (Fig. 1). Following removal of the haem from CB5, CoSalen was bound to the protein scaffold to form an ArM (Fig. 1A). In the present work, we prepared and characterized catalytically relevant amounts of the water-soluble CB5:CoSalen ArM and studied its ability to drive homogeneous WO in photocatalytic conditions. We found that when prepared in specific conditions this ArM is indeed capable of driving photocatalytic WO in the presence of $[Ru(bpy)_3](ClO_4)_2$ as photosensitizer and $Na_2S_2O_8$ as sacrificial electron acceptor. Further, we present a detailed analysis of the stability and decomposition pathways of this photocatalytic system, as understanding the side reactions that may occur when ArMs are exposed to the severe conditions of photocatalytic WO is required to derive future ArMs for solar fuel production.

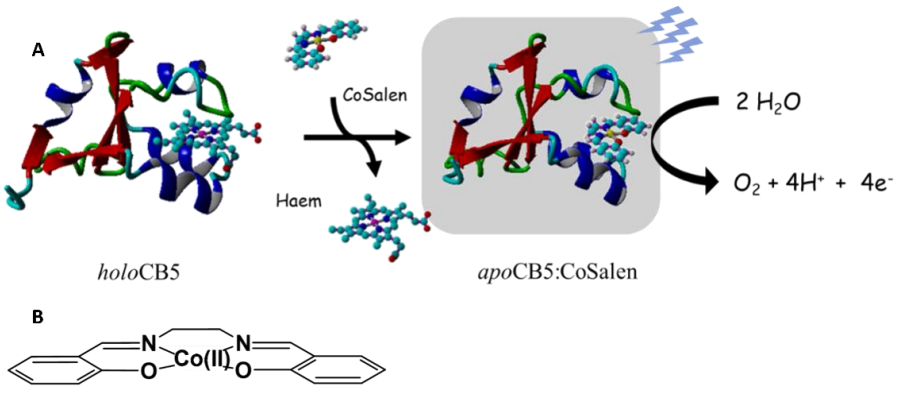

*Figure 1: **A** General scheme for the production of photoactive CB5:CoSalen artificial proteins. HoloCB5 (left, PDB: 1CYO), and apoCB5:CoSalen 1:1 (right, model created using protein visualization software YASARA) [55]. **B** The structure of CoSalen.*

2 RESULTS

2.1 Preparation and binding stoichiometries

To prepare the CB5:CoSalen ArM, the haem cofactor of CB5 was removed using Teale's method. This method consists of dissociating haem by lowering the pH of the protein solution to 2 and removing the released haem with an organic solvent. This was followed by a buffer exchange to 20 mM NaPi (sodium phosphate) at pH 8.0, first *via* dialysis and then by a desalting column. Then, different ArM samples were prepared by reacting the resulting *apo*protein (*apo*CB5) with 1 or 5 equivalents of CoSalen at 4 °C. The effective stoichiometry of the isolated samples, *i.e.*, the CB5:CoSalen molar ratio of the ArM, was determined experimentally using inductively coupled plasma mass spectrometry (ICP-MS) for measuring the metal concentration, and a BCA kit (bicinchoninic acid kit) for quantifying the protein concentration. For the sample prepared with 1 eq. of CoSalen, the final *apo*CB5:CoSalen ratio varied from 1:0.6 to 1:0.8, while for those prepared with 5 eq. CoSalen the final *apo*CB5:CoSalen ratio was 1:4. As a control, samples were prepared by reacting the *holo*CB5 protein (*i.e.*, the protein still bearing its haem cofactor) with 5 eq. CoSalen. The corresponding haem-containing samples showed a lower CB5:CoSalen ratio of 1:3. Taken together, the results suggest that in the *apo*CB5:CoSalen 1:5 samples, CoSalen may bind both to the haem binding site and to alternative, yet undefined, binding sites. To investigate whether *apo*CB5:CoSalen samples contained a dynamic equilibrium of bound and unbound CoSalen, especially those in which binding ratios >1 was observed, *apo*CB5:CoSalen 1:5 samples were passed thrice over a micro spin Bio-Rad P6 column, and the *apo*CB5:CoSalen ratio was measured after each passage. The ratio did not vary significantly between passages (Table S1), which was a clear indication that all CoSalen molecules were stably attached to the protein scaffold. As a note, in the remainder of the article we will call these samples *apoCB5:*CoSalen 1:1 and *apoCB5:*CoSalen 1:5, referring to the stoichiometry of the reaction performed for their preparation.

2.2 Spectroscopic characterization

The purified CB5:CoSalen samples were characterized by UV-vis spectroscopy (Fig. 2A-C). In each CB5:CoSalen sample spectral characteristics

of both CB5, the π-π* bands, and CoSalen, the d-d and MLCT bands were observed. Upon interacting with *apo*- or *holo*CB5 small shifts in the d-d band of the CoSalen complex from 368 nm to 377 nm were observed, as well as a red-shift of the MLCT band from 235 nm to 257 nm. Both shifts indicated a change in the coordination environment of the metal complex. The above observations taken together suggested that CoSalen had indeed been coordinated by CB5. Finally, as seen in Fig. 2C, the binding of CoSalen to *holo*CB5 did not lead to loss of the coordinated haem, as the haem Soret band at 413 nm and Q bands at 532 nm and 560 nm were unaffected. The binding of CoSalen to both *apo*- and *holo*CB5 was further investigated by electrospray ionization mass spectrometry (ESI-MS, see Fig. S3). As discussed in Chapter 2 a peak characteristic of the *apo*CB5 protein (mass = 10093 Da, calculated (*calc)* mass = 10093 Da), as well as a peak characteristic of *apo*CB5:CoSalen 1:1 (mass = 10417 Da, *calc* = 10418 Da), were observed in the samples prepared from 1:1 mixtures, while in samples prepared from 1:5 mixtures up to 3 CoSalen complexes were found bound to *apo*CB5 (mass = 11066 Da, *calc* mass = 11068 Da). The control samples prepared from *holo*CB5 and 5 eq. of CoSalen showed peaks corresponding to *apo*CB5 (mass = 10093 Da), *apo*CB5:CoSalen 1:1 (mass = 10417 Da), and *apo*CB5:CoSalen 1:2 (mass = 10741 Da, *calc* mass = 10743 Da), suggesting that the histidine-haem binding did not survive the conditions of the ESI-MS analysis and that the *apo*CB5:CoSalen interaction is stronger than the *apo*CB5-haem interaction under ESI-MS conditions.

Circular dichroism (CD) was used to determine the influence of CoSalen binding on protein folding (Fig. 2D-F). To discuss CD spectra, it is practical to consider the protein structure. Homology models of both proteins *apo*- and *holo*CB5 were generated using the Swiss Model software (Fig. 3) [56–60]. *Holo*CB5 contains a beta-sheet core and 5 alpha helices, 4 of which frame the haem binding pocket. Haem is coordinated by two histidines, H44 and H68, in axial position to iron. According to this homology model upon haem removal, the alpha-helical character around the binding site was lost,[61] while the beta-sheet core remained mostly intact [62].

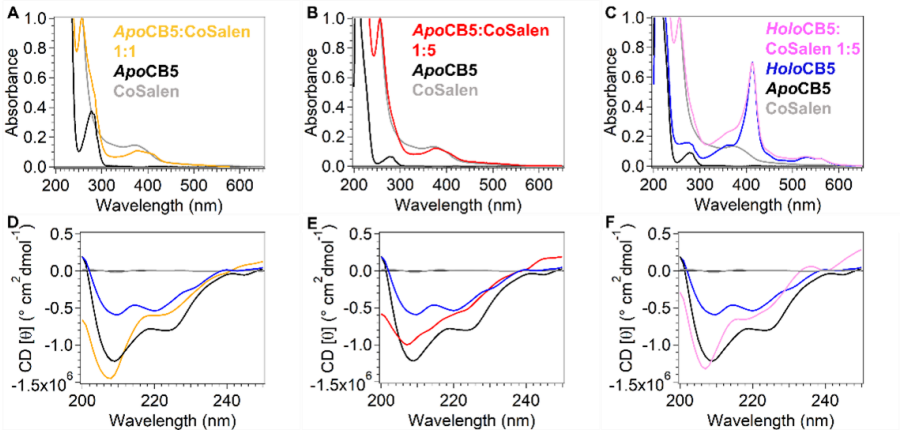

*Figure 2: UV-vis (**A-C**) and CD (**D-F**) spectra of from left to right, apoCB5:CoSalen 1:1 (**A, D**), apoCB5:CoSalen 1:5 (**B, E**) and holoCB5:CoSalen 1:5 (**C, F**). In each spectrum, apoCB5:CoSalen 1:1 (orange), apoCB5:CoSalen 1:5 (red), holoCB5:CoSalen 1:5 (pink), holoCB5 (blue), apoCB5 (black), and CoSalen (grey). In the UV-vis spectra the spectra of apoCB5 and holoCB5 were normalized to match the protein concentration determined for the CB5:CoSalen sample in the same panel, and the spectra of the CoSalen cofactor alone were normalized to the cobalt concentration in the CB5:CoSalen sample.*

The CD spectrum of *apo*CB5 contained a mixture of beta-sheet, unfolded strand, and alpha-helix, character (Fig. 2) as expected from the computed structure shown in Fig. 3 [63]. Upon reacting CoSalen with *apo*CB5 in a 1:1 ratio a slight loss of alpha-helical character occurred with respect to *apo*CB5, while the alpha-helical contribution was further reduced for samples reacted at a 1:5 ratio, which binds multiple CoSalen per protein (Fig. 2D and E). The CD spectrum of *holo*CB5:CoSalen 1:5 was found to be very similar to that of *apo*CB5:CoSalen 1:1 (Fig. 2F) suggesting that a significant loss of alpha-helical fold took place upon binding of CoSalen to *holo*CB5, to lead to a protein folding similar to that of *apo*CB5:CoSalen 1:1. The loss of alpha-helical fold observed in *holo*CB5:CoSalen, compared to *holo*CB5, and of *apo*CB5:CoSalen 1:5, compared to *apo*CB5:CoSalen 1:1, indicated that the binding of CoSalen to the protein exterior had a destabilizing effect on the protein alpha-helical structure.

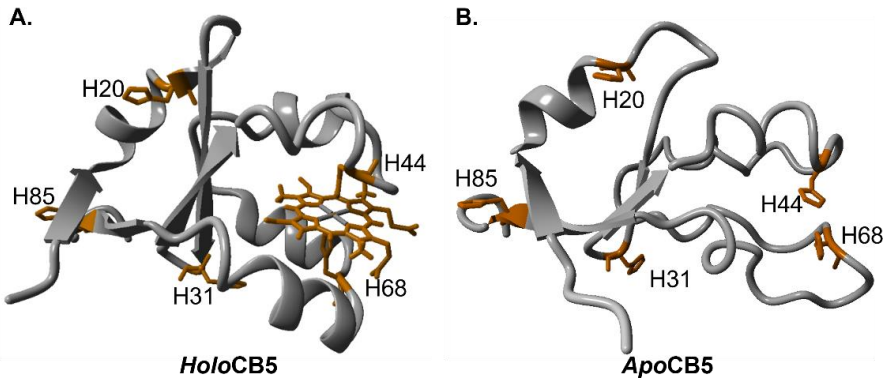

*Figure 3: Homology model of holoCB5 (**A**) and apoCB5 (**B**) showing each histidine explicitly (the homology models were prepared as detailed in the supplementary section).*

As the protein scaffold contains a single, fluorescent tryptophan residue (W27) located near one of the coordinating histidines (H20, see Fig. S4), steady-state fluorescence spectroscopy was also used to analyse the interaction between CoSalen and *apo*CB5 in *apo*CB5:CoSalen samples. The fluorescence emission of tryptophan varies from 330 nm to 350 nm, depending on the hydrophobicity of its local environment [64]. Inside redox proteins, for example, tryptophans can be involved in electron transfer reactions, and its fluorescence fingerprint has been used to study excitation energy transfer and redox reactions in biological systems [65–67]. In addition, some transition metals have been reported to quench fluorescence emission in proteins [68–74]. The effect of CoSalen binding on the tryptophan fluorescence of CB5 is shown in Fig. 4. The maximum emission of W27 from *apo*CB5 was found at 340 nm. The fluorescence in *holo*CB5 was quenched with respect to *apo*CB5, which is a known consequence of the paramagnetic iron centre of the haem porphyrin acting as an emission quencher [75,76]. Similarly, the emission of *apo*CB5:CoSalen 1:5 was less intense than that of *apo*CB5:CoSalen 1:1, which was less intense than for *apo*CB5 at 340 nm. We hypothesize this observation to be a consequence of W27 fluorescence quenching by the bound cobalt complex, which was confirmed by following the intensity of the peak at 415 nm, which originates from the presence of CoSalen, in a titration experiment (Fig. S5). We further noted a blueshift in the fluorescence maxima of both *apo*CB5:CoSalen 1:1 and 1:5, compared to that of *apo*CB5 with maxima at 336 and 327 nm,

respectively. The fluorescence spectra of *apo*CB5:CoSalen resembled the characteristics of the fluorescence spectrum of *holo*CB5, with maxima at 337 nm, better than the spectra of *apo*CB5, in terms of low emission by quenching and its blue-shifted maximum (Fig. 4). The observed blueshift indicates an increase in the hydrophobicity of the tryptophan environment, especially for *apo*CB5:CoSalen 1:5. These observations indicate that the fluorescence quenching of W27 is due the presence of CoSalen in the protein, since the binding of more CoSalen results in more quenching, and the fluorescence blue shift indicates a transition of W27 towards a more hydrophobic environment in the presence of CoSalen, which might be provided by coordination of CoSalen to H20 located close to W27 (see Fig. S4).

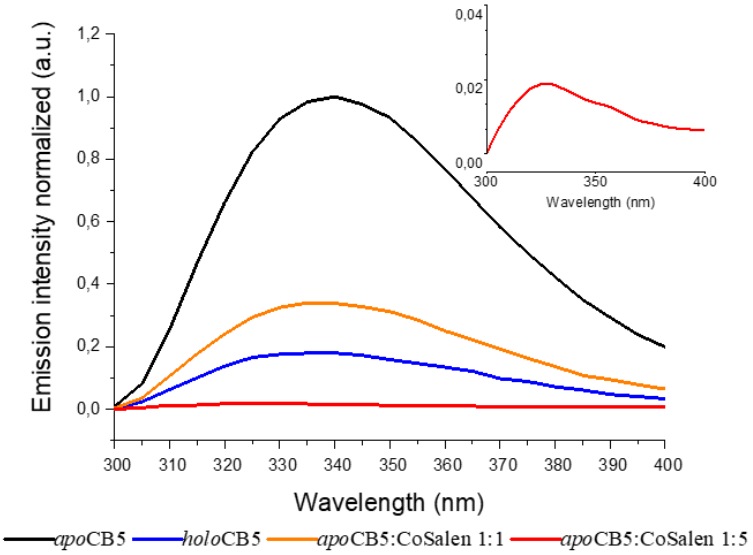

Figure 4: Plot of steady-state fluorescence emission of the W27 residue in apoCB5 (black), holoCB5 (blue), apoCB5:CoSalen 1:1 (orange) and apoCB5:CoSalen 1:5 (red) when excited at 280 nm. Inlet: Spectrum of apoCB5:CoSalen 1:5 adduct emission from 300 to 400 nm.

Size exclusion chromatography multi-angle light scattering (SEC-MALS) was used to analyse potential protein-protein interactions in the CB5:CoSalen samples (Fig. 5). *Apo-* and *holo*CB5 were both found to be primarily monomeric. In the *apo*CB5:CoSalen 1:1 sample, the protein was essentially

monomeric, and minor fractions of dimers and octamers were observed. Finally, in the 1:5 samples, the monomeric peak was the major species, and in addition a significant population of multimers was found. The overall reaction of 1 eq. of the CoSalen complex with *apo*CB5 appears to alter to a minor extent the aggregation state of the protein, while the addition of 5 equivalents of CoSalen led to significant multimerization, which may result from the coordination of two exterior histidine residues of two different proteins to the same CoSalen complex.

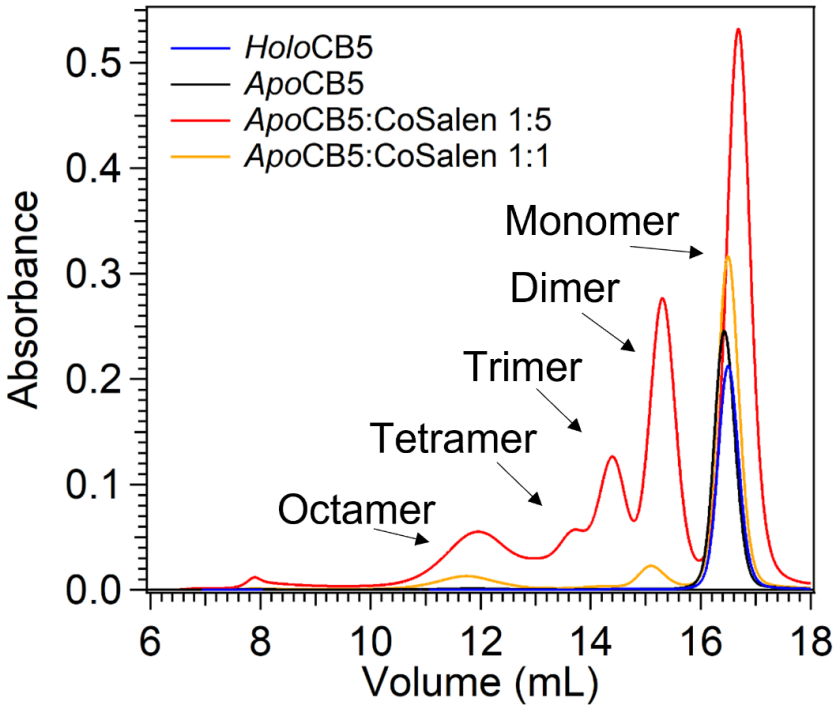

Figure 5: SEC-MALS analysis of holoCB5 (blue), apoCB5 (black), apoCB5:CoSalen 1:5 (red) and apoCB5:CoSalen 1:1 (orange). The assignment of the aggregation state of each peak, based on MALS data (not shown), is indicated in the figure.

2.3 Binding location and oxidation state of CoSalen bound to CB5

Metalloproteins typically bind metal-based cofactors *via* histidine residues. To better characterize the binding site of CoSalen to CB5, histidine side chain-focused ^{15}N-^{1}H heteronuclear single quantum coherence spectroscopy (HSQC) NMR with a large spectral window (LSW HSQC) was performed on *apo*CB5, *apo*CB5:CoSalen 1:1, and *apo*CB5:CoSalen 1:5 (Fig. 6). As shown in the homology models in Fig. 3, CB5 contains 5 histidine residues. The H44 and H68 are in the haem binding pocket and H20, H31, and H85 are on the protein exterior. Site-directed mutagenesis of the outer histidine residues of *apo*CB5 was first used for their assignment (Tables S2 and S3). In this manner, the outer residues H31 and H85, as well as binding pocket residues H44 and H68 could be assigned in the LSW HSQC spectrum. H20 was not observed in the LSW HSQC spectrum.

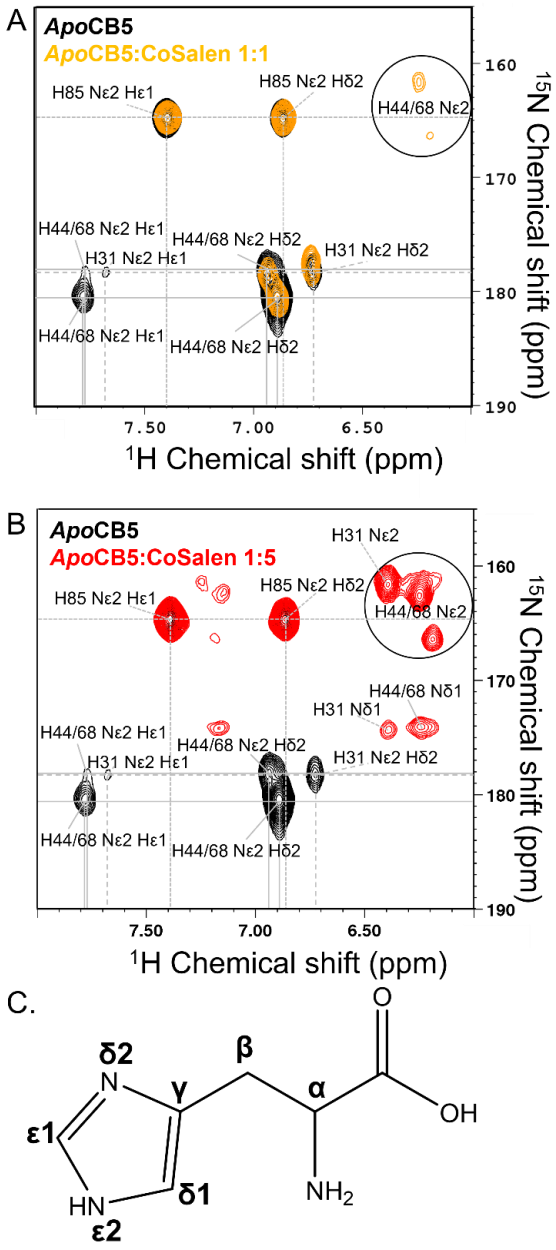

*Figure 6: LSW 15N-1H HSQC NMR of apoCB5 (black), apoCB5:CoSalen 1:1 (**A**, orange) and apoCB5:CoSalen 1:5 (**B**, red). Peak assignments are shown in the figure and in tables S2 and S3, with the labelling of the histidine ring as in **C**.*

Second, the pK_a value of each histidine residue in *apo*CB5 was determined using a 5-point pH titration from pH 6 to 8 (Fig. S6). The chemical shifts obtained were fitted using equation (1)

$$\delta_{obs} = \frac{\delta_L + \delta_{HL} * 10^{pH - pKa}}{1 + 10^{pH - pKa}} \quad 1$$

In which δ_{obs} is the observed chemical shift and δ_L and δ_{HL} are the limiting chemical shifts of the deprotonated and protonated states, respectively. Data fitting led to a pK_a of 6.4 for H31 and 6.7 for both binding pocket histidines H44 and H68, while H85 was not affected by the change in pH over the measured range. Third, the LSW HSQC spectra for *apo*CB5:CoSalen 1:1 and 1:5 were measured. For *apo*CB5:CoSalen 1:1 the peak intensities of H44 and H68 decreased, while two upfield-shifted peaks emerged (Fig. 6A). For *apo*CB5:CoSalen 1:5 both histidine peaks corresponding to the binding pocket (H44/H68), as well as the H31 peaks, were shifted upfield, while the original peaks present in *apo*CB5 disappeared (Fig. 6B). The observed peak shifts for *apo*CB5 samples reacted with CoSalen differed from the shifts measured during pK_a measurements, thus excluding that the former would be caused by a change in the protonation state of the histidine residues (Fig. S6, Fig. 6). The observed changes could then be related to the binding of CoSalen to histidine, a change in the oligomeric state as observed in Fig. 5, or a change in the tertiary structure of the protein as seen in Fig. S7 and Fig. 2. The observed changes cannot exclusively be related to changes in the oligomeric state as SEC-MALS in Fig. 5 revealed that CB5:CoSalen is still primarily in the monomeric state, while in LSW NMR the binding pocket and H31 peaks are completely shifted in this sample. Furthermore, large oligomers cannot be measured with solution NMR. While changes in tertiary structure cannot be excluded as the reason for the observed peak shifts both ESI-MS and SN-gel electrophoresis support the binding of CoSalen in the binding pocket of *apo*CB5 in the 1:1 and 1:5 samples. Both techniques confirm binding of CoSalen to CB5. SN-PAGE supports binding in the binding pocket by indicating increased sample stability upon complex binding, Chapter 2, section 4. ESI-MS in Chapter 2, section 3.3 supports binding in the binding pocket since binding of axial CO was only observed when more than 1 CoSalen was bound to CB5. In other words, the NMR results indicate that for *apo*CB5:CoSalen 1:1 samples, coordination of CoSalen with H44 and H68 took place in the binding pocket, while reaction in a 1:5 ratio of

*apo*CB5:CoSalen also led to the coordination of CoSalen to H31. Since the two peaks assigned to H44/H68 moved together upon reaction with CoSalen, we hypothesize that they are coordinating CoSalen in the same manner, so that CoSalen is hexacoordinated in the *apo*CB5 binding pocket between H44, H68, and $Salen^{2-}$. It should be noted here that while no binding of CoSalen to H85 has been observed by NMR, and H20 remained invisible in all NMR spectra, ICP-MS data (see above) indicated that up to 4 CoSalen complexes can bind to CB5 in the 1:5 samples, which suggests that H85 or H20 may bind to cobalt.

The NMR spectra of the CB5:CoSalen ArMs suggest a diamagnetic Co(III) oxidation state since line broadening or strong downfield shifts upon binding of His to cobalt were not observed (Fig. 6 and Fig. S7). Continuous wave EPR was performed to determine the oxidation state of CoSalen in *apo*CB5:CoSalen 1:1 and 1:5 samples. CoSalen in solution was also measured, both in aqueous buffer and in chloroform (Fig. 7A and B). In an aqueous environment, CoSalen was found to be high spin Co(II) (S = 3/2) [77,78] while in chloroform the complex was found to be in the low spin Co(II) state (S=1/2) [79]. This difference may be related to the presence of some Cl^- in chloroform, which may coordinate CoSalen axially, introducing a stronger ligand field. The spectra acquired for *apo*CB5:CoSalen 1:5 (Fig. 7C and D), with cobalt concentrations comparable to those used for the free CoSalen, did not give any EPR signal attributable to cobalt species (Fig. 7C and D, red spectrum), in spite of the use of signal enhancing conditions (*e.g.,* high power, high modulation amplitude, low temperature). We therefore hypothesized that CoSalen was in the EPR silent Co(III) state when bound to CB5. To test this hypothesis the 1:5 sample was subjected to reduction by ascorbic acid before re-measuring an EPR spectrum (Fig. 7D, black spectrum). In this case, the spectrum resembled the one obtained for the CoSalen dissolved in the NaPi buffer of a high spin Co(II) state (Fig. 7A). After a chromatography step that would remove any unbound CoSalen, ICP-MS showed cobalt concentrations compatible with CB5 being fully complexed by CoSalen, proving that the Co-EPR signal observed after reduction derives from CoSalen bound to CB5. In conclusion, the EPR results are fully consistent with the picture that CoSalen is bound to CB5 in the diamagnetic Co(III) oxidation state, in agreement with NMR data.

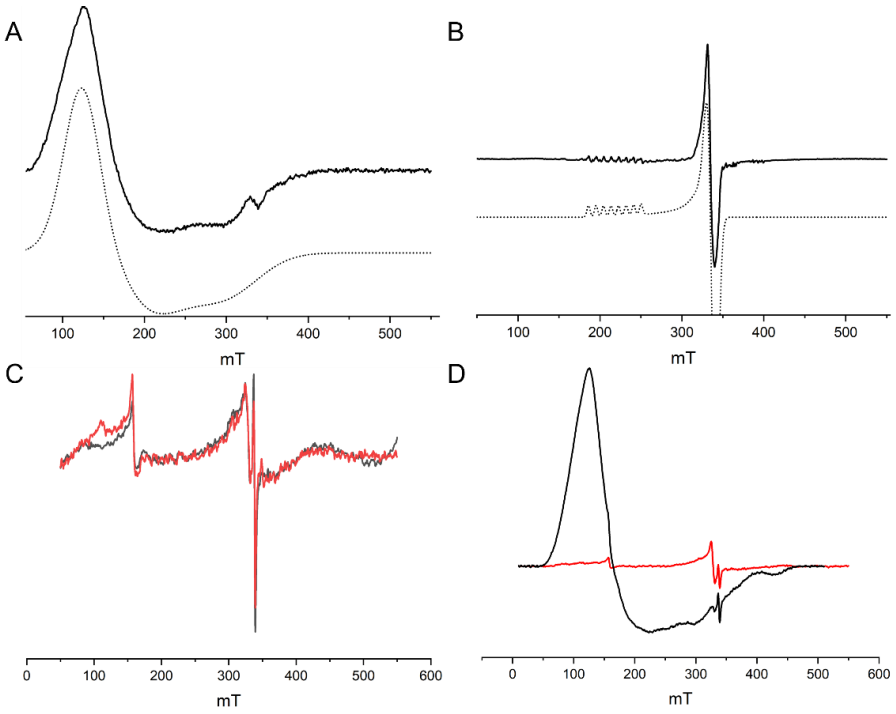

Figure 7: Low temperature EPR spectra of CoSalen complex in solution and complexed with apoCB5. ***A*** *CoSalen in aqueous buffer (solid line, black) and simulation as Co(II) S=3/2 (dashed line, grey).* ***B*** *CoSalen in chloroform (solid line) and simulation as Co(II) S=1/2 (dashed line).* ***C*** *apoCB5:CoSalen 1:5 ratio (red) and apoCB5 (black).* ***D*** *apoCB5:CoSalen 1:5 ratio (red) and after reduction with ascorbic acid (black). Signals in* ***C*** *are attributed to cavity background and spurious paramagnetic impurities. For details on experimental parameters and simulations, Supplementary Information.*

2.4 Water oxidation photoactivity of CB5:CoSalen samples

Once characterized, the capacity of the *apo*- and *holo*CB5:CoSalen ArM samples to oxidize water photocatalytically was tested in presence of $[Ru(bpy)_3](ClO_4)_2$ as photosensitizer (PS) and $Na_2S_2O_8$ as sacrificial electron acceptor (SA) in a sodium phosphate buffer (80 mM) at pH 7.5 (for full experimental setup, see Supplementary Information). Fig. 8 represents the O_2 evolution of free CoSalen, *apo*CB5 (control), *apo*CB5:CoSalen 1:1, *apo*CB5:CoSalen 1:5, and *holo*CB5:CoSalen 1:5.

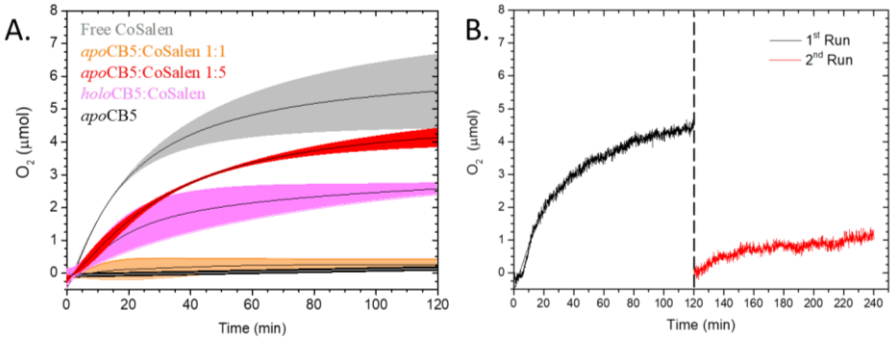

Figure 8: ***A*** *Photocatalytic O_2 evolution by apoCB5:CoSalen 1:1 (orange), apoCB5:CoSalen 1:5 (red), holoCB5:CoSalen 1:5 (pink), apoCB5 (black) and free CoSalen (grey). Conditions: [catalyst] 50 µM in Co, $[Ru(bpy)_3](ClO_4)_2$ 0.3 mM, $Na_2S_2O_8$ 5 mM, 80 mM NaPi pH 7.5, 25°C, 450 nm LED (18-19 mW). For apoCB5, concentration was based on protein (50 µM).* ***B*** *O_2 evolution activity of apoCB5:CoSalen 1:5. The sample was irradiated for a total of 240 min. Irradiation started at t = 0 min. For the first run (black) the sample was irradiated with 450 nm LED (18-19 mW) in photocatalytic conditions: [catalyst] 50 µM in Co, $[Ru(bpy)_3](ClO_4)_2$ 0.3 mM and $Na_2S_2O_8$ 5 mM, 80 mM NaPi pH 7.5, 25°C. After 120 min, irradiation was stopped and more $[Ru(bpy)_3](ClO_4)_2$ and $Na_2S_2O_8$ was added (same concentrations, dashed line). After addition of another identical quantity of PS and SA, a second run (red) was started, and the sample was irradiated for another 120 min. All experiments were performed in duplo. Data were fitted using OriginPro software. For raw data of panel,* ***A****, see Figure S8 in Supplementary Information.*

As a reference, O_2 evolution activity of free CoSalen was recorded under identical photocatalytic conditions. Free CoSalen produced 5.57±0.85 µmol of O_2 over 120 min irradiation (grey trace, Fig. 8A). Afterwards, the photoactivity of *apo*CB5 was tested. With this sample no dioxygen production was observed, indicating that this protein was not capable of catalysing such a reaction (black trace, Fig. 8A). For the sample containing *apo*CB5:CoSalen 1:1 as a catalyst, no O_2 production was detectable either (orange trace, Fig. 8A). In contrast, the sample containing *apo*CB5:CoSalen 1:5 was found to be catalytically active producing 4.24±0.24 µmol of dioxygen with a turnover number (*TON*) of 24 (red trace, Fig. 8A, Table S4). This performance was comparable, in terms of stability, with that of free

CoSalen (*TON* 31, Table S4), but the maximal turnover frequency (TOF_{max}) of *apo*CB5:CoSalen 1:5 (0.63 min^{-1}) was approximately half compared to that of CoSalen (1.36 min^{-1}) (Table S4). *Holo*CB5:CoSalen 1:5 generated less O_2 (pink trace, Fig. 8A), as characterized by a twice lower *TON* of 16, but only a slightly lower TOF_{max} of 0.55 min^{-1} (Table S4). On the one hand, these results are one of the first demonstrations that artificial proteins can perform photocatalytic water oxidation. On the other hand, the mechanism of such a reaction is far from obvious, and in particular the question of whether the CoSalen-protein complex stayed intact under photocatalytic conditions, remained fully open at this stage. Loss of the cobalt could lead to catalysis performed by cobalt nanoparticles, cobalt-containing small molecules, or some form of cobalt-bound protein species.

Finally, to test whether the *TON* of *apo*CB5:CoSalen 1:5 was limited by the lifetime of the ArM or that of the photosensitizer or sacrificial agent, the photocatalysis was continued by addition of fresh PS and SA after the activity had ceased (Fig. 8B). The addition of fresh PS and SA did lead to a continuation of the dioxygen production, though the amount generated was significantly lower than that of the initial run. No precipitation was observed in the solution during the second run. Overall, this experiment proved that the activity of *apo*CB5:CoSalen 1:5 was limited essentially by the PS or SA as is the case for free CoSalen,[80] but suggested that the ArM was affected in such conditions.

2.5 Nanoparticle formation and ligand release

To test the stability of the *apo*CB5:CoSalen complex 1:5 under photocatalytic conditions, ICP-MS analysis was performed for samples at different irradiation times, *i.e.*, before, and after 0.5 min, 3 min, and 120 min irradiation in the presence of sacrificial agent and photosensitizer (Fig. 9).

Each sample was run over a microspin Bio-Rad P6 size exclusion column to remove any released, small-molecule CoSalen. The initial *apo*CB5:CoSalen stoichiometry was 1:4.0 (see above). After 3 min of irradiation in the presence of PS and SA, this number dropped to 1:1.2, indicating that only one CoSalen remained bound. After 120 min of irradiation, the average number of CoSalen *per* CB5 had dropped down to 0.2, suggesting that little CoSalen was bound to the protein scaffold. Overall, the ICP-MS data revealed that the majority of CoSalen cofactors detached from CB5 within 10 min of blue light

irradiation. Since water oxidation activity continued for approximately 120 min, we suspect that the photocatalytically active compound is not the original *apo*CB5:CoSalen adduct (see discussion).

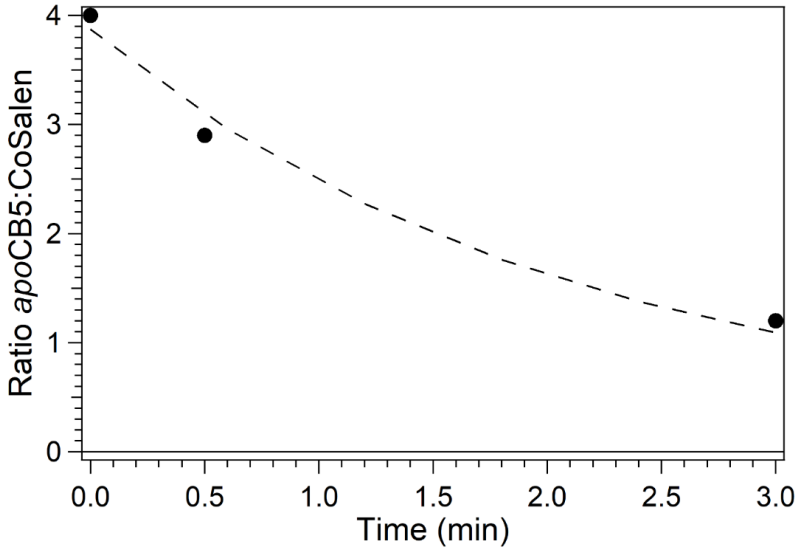

Figure 9: The stability of apoCB5:CoSalen 1:5 under photochemical conditions. The ratios of the amount of cobalt per CB5, determined by ICP-MS and a BCA kit after purification over a microspin Bio-Rad P6 column, are plotted for the apoCB5:CoSalen 1:5 sample, and after 0.5 min and 3 min of irradiation at 450 nm in the photoreactor setup (see Supporting Information for setup) in the presence of $[Ru(bpy)_3](ClO_4)_2$ and $Na_2S_2O_8$ (dots) with an exponential fit (dashed line).

For photocatalytic water oxidation using free CoSalen as a catalyst, $[Ru(bpy)_3]^{2+}$ as photosensitizer, and $Na_2S_2O_8$ as sacrificial electron acceptor, it is known that the molecular complex CoSalen is a pre-catalyst of the catalytically active species and that the activity of this system can be ascribed to a mixture of cobalt oxide and cobalt hydroxide nanoparticles [16,80]. To investigate if such nanoparticles were also formed in our artificial protein system during photocatalysis, dynamic light scattering (DLS) analysis was performed on photocatalytic mixtures containing *apo*CB5:CoSalen 1:1, *apo*CB5:CoSalen 1:5, *holo*CB5:CoSalen 1:5, or free CoSalen as a catalyst, $[Ru(bpy)_3](ClO_4)_2$ and $Na_2S_2O_8$ in a phosphate buffer solution at pH 7.5. Samples were measured three times: i) at t = 0, ii) after keeping the mixture

in the dark for 120 min, and iii) after blue light irradiation for 120 min (Fig. 10 and S17).

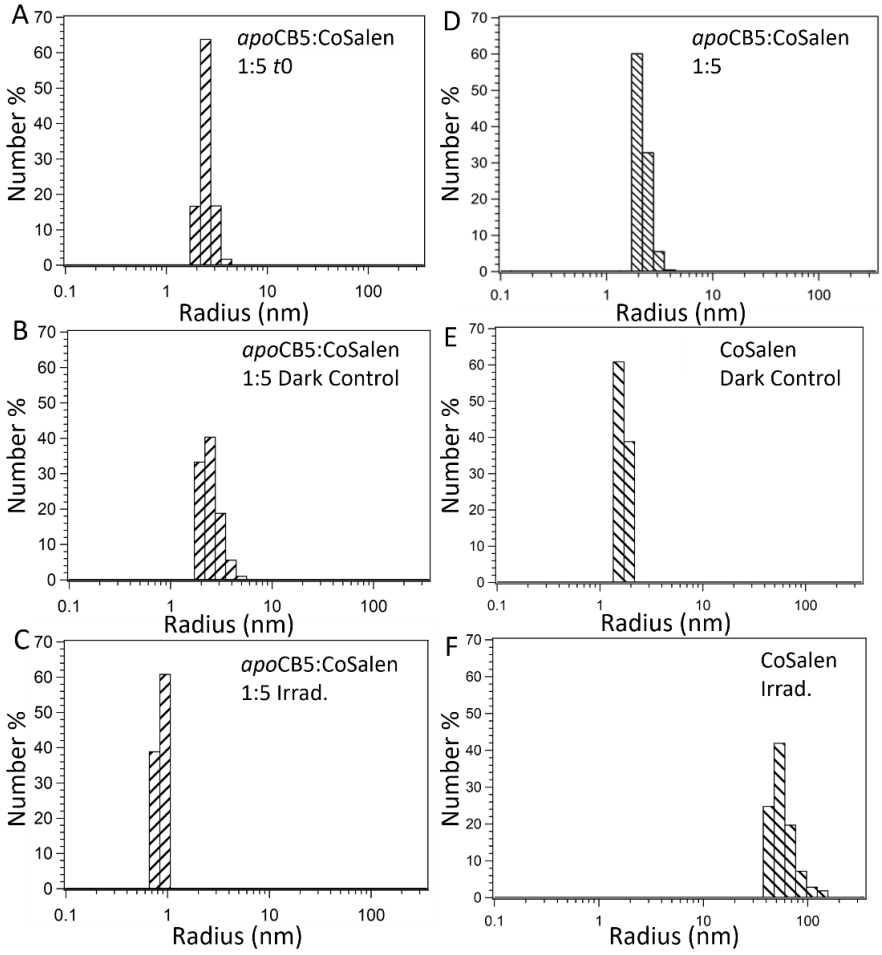

*Figure 10: Dynamic light scattering (DLS) analysis for apoCB5:CoSalen 1:5 and free CoSalen samples, kept in the dark or irradiated with blue light. Y-axis indicates the percentage of the number of particles. All sample contained 50 µM CoSalen, either free or bound to CB5, in 80 mM NaPi pH 7.5 buffer. The following distributions can be observed: apoCB5:CoSalen 1:5 directly after addition of PS and SA (**A**), apoCB5:CoSalen 1:5 + PS + SA after 120 min incubation in the dark (**B**), apoCB5:CoSalen 1:5 + PS + SA after 120 min irradiation (**C**), apoCB5:CoSalen 1:5 alone (**D**), free CoSalen + PS + SA kept in the dark (**E**), and free CoSalen + PS + SA after 120 min irradiation (**F**).*

Conditions: $[Ru(bpy)_3](ClO_4)_2$ (PS); 0.3 mM, $Na_2S_2O_8$ (SA):5 mM, T = 25 °C, light source 450 nm, 18-19mV.

The sample containing free CoSalen, PS, and SA kept in the dark formed small nanoparticles with a diameter of around 1-2 nm. After light irradiation for 120 min, the formation of larger nanoparticles was detected, characterized by an average diameter of 47 nm. The behaviour of the *apo*CB5:CoSalen samples containing PS and SA was rather different. Before and after irradiation, the particle size was around 2 nm, indicating that contrary to the free molecular catalyst, for the ArM catalyst no nanoparticles were observed. To test if intact H_2Salen ligands may be part of the soluble species present in solutions after photocatalysis, a high-resolution mass spectrum (HR-MS) was measured in the positive mode to detect small molecules. Two solutions in presence of $[Ru(bpy)_3](ClO_4)_2$ and $Na_2S_2O_8$ after 120 min irradiation were analysed: a) *apo*CB5:CoSalen 1:5 and b) free CoSalen (Fig. S9–S10,). Free H_2Salen ligand was observed (*m/z* = 268) in the solutions for each case upon light irradiation in the presence of PS and SA, indicating that in both cases of free CoSalen and of the active *apo*CB5:CoSalen 1:5 catalyst, the Salen ligand had been released within 120 min irradiation.

2.6 Stability of the CB5:CoSalen in the presence of a photosensitizer (PS) and sacrificial electron acceptor (SA).

The photostability of the *apo*CB5:CoSalen samples was first studied in absence of PS and SA. The UV-vis spectrum of a solution containing 50 µM of either *apo*CB5:CoSalen 1:1 or 1:5 in 80 mM phosphate buffer at pH 7.5 was recorded *vs.* time under constant irradiation with a 450 nm light source (Fig. S11A and B). After 120 min of continuous irradiation, the spectra of both samples, *apo*CB5:CoSalen 1:1 and *apo*CB5:CoSalen 1:5, did not show any visible changes. In addition, high-resolution mass spectra of the above samples, measured after irradiation, showed the presence of CoSalen (*m/z* = 325.04) and the complex: protein adduct, *i.e. m/z* = 869 for *apo*CB5:CoSalen 1:1 sample and *m/z* = 1230 for *apo*CB5:CoSalen 1:3, and no trace of the free Salen ligand could be identified (Fig. S12-S13). In addition, semi-native and denaturing gel electrophoresis analysis of the irradiated *apo*CB5:CoSalen 1:1 and 1:5 samples showed the stability of the protein under irradiation (Fig.

S11C). Overall, we concluded that *apo*CB5:CoSalen 1:1 and *apo*CB5:CoSalen 1:5 samples are stable under blue light irradiation.

The next step consisted of studying the protein-cobalt adduct integrity in presence of the PS and SA. Fluorescence emission spectroscopy was employed to determine if *apo*CB5:CoSalen 1:1 and 1:5 were also stable upon irradiation in the presence of the PS and SA in 80 mM NaPi pH 7.5 buffer (Fig. 11). The irradiated samples, containing *apo*CB5:CoSalen 1:1 or 1:5 in presence of PS and SA, were compared with the samples before irradiation. Upon irradiation, after one photocatalytic run, the tryptophan fluorescence emission of either the *apo*CB5:CoSalen 1:1 or the *apo*CB5:CoSalen 1:5 sample was no longer visible. This result suggests that under the harsh conditions of photocatalysis, chemical/structural changes did occur at the protein Trp site.

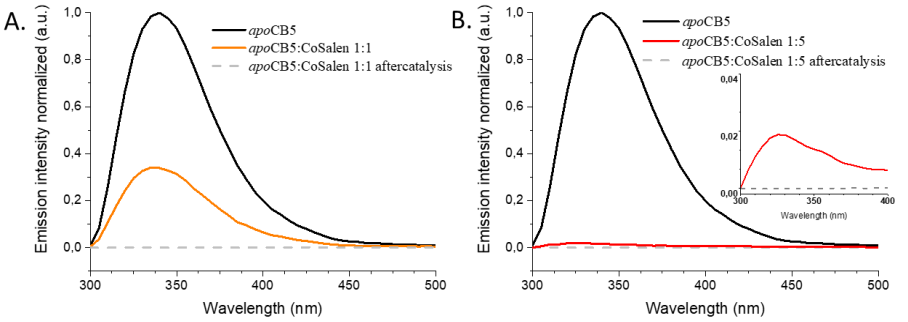

*Figure 11: Tryptophan fluorescence emission spectra of apoCB5:CoSalen samples before and after photocatalysis under 18-19 mW irradiation at LED 450 nm. ApoCB5 (black), apoCB5:CoSalen 1:1 + PS + SA before (orange) and after photocatalysis (grey) (**A**). ApoCB5 (black), apoCB5:CoSalen 1:5 + PS + SA before (red) and after photocatalysis (grey) (**B**). Insert: Detailed view of apoCB5:CoSalen 1:5 adduct emission from 300 to 400 nm before and after catalysis. Excitation: 280 nm. conditions: PS = 0.3 mM $[Ru(bpy)_3](ClO_4)_2$, SA = 5 mM $Na_2S_2O_8$, [Cat] = 50 µM in Co, 25 °C, 3.5 mL, 80 mM NaPi pH 7.5.*

ESI-MS spectra of *apo*CB5:CoSalen 1:1, 1:5, *holo*CB5:CoSalen 1:5, and *apo*CB5 were measured in the presence of PS and SA, directly after sample preparation or following 120 min incubation in the dark. The spectra of the samples before and after incubation in the dark were found to be quite similar (Fig. S14). To study the effect of PS and SA on the protein in the dark, gel electrophoresis was employed. On SDS-PAGE (Fig. S15) *apo*CB5:CoSalen 1:1 runs at the same height as *apo*CB5. However, on semi-native gel (Fig. S15)

two populations could be distinguished in *apo*CB5:CoSalen 1:1, one running at the height of *apo*CB5 and one running below it, the latter being assigned as reacted CB5:CoSalen [54]. The mass spectrum and SDS-PAGE of the solution containing *holo*CB5:CoSalen looked very similar to *apo*CB5:CoSalen 1:1. The sample containing *apo*CB5:CoSalen 1:5, on the other hand, showed a ladder of multimers on semi-native gel in accordance with SEC-MALS (Fig. 5). The appearance of multimers in the purified CB5:CoSalen sample on the semi-native gel in Figure S15B in this Chapter, which were not observed in lane 2 compared to Fig. 2 Chapter 2 is likely the result of the lower concentration used on the gel in Chapter 2, 20 µM vs. 10 µM. However, it may also be a result of the removal of DMF during the purification step or higher concentration of the stock of the former sample in this Chapter. The multimer bands observed in the semi-native gel of *apo*CB5:CoSalen 1:5 (Fig. S15B, lane 2, left image) did not show on denaturing gel (Fig. S15B, lane 2, right), as they are not strong enough to withstand the denaturing conditions in presence of SDS and β-mercaptoethanol. In contrast, SDS-page of samples taken of *apo*CB5:CoSalen 1:5 directly after addition of PS and SA to the solution (Fig. S15B, lane 3), also showed bands of dimers and trimers on denaturing gel, and further aggregation, seen as fading of the monomer band, was observed after 120 min dark incubation with PS and SA (Fig. S15B, lane 4, right). This observation suggests a limited cross-linking effect of PS and SA on the CB5 protein observed after dark incubation (see discussion section below). With the *apo*CB5:CoSalen 1:1 sample, multimers were only observed on denaturing gel after 120 min incubation with PS and SA in the dark. For *holo*CB5:CoSalen, the cross-linking effect was not observed.

To investigate the photostability of our most active artificial protein system, *apo*CB5:CoSalen 1:5 was studied after irradiation in the presence of PS and SA. Both mass spectroscopy and gel electrophoresis were performed (Fig. S16) and the samples were tested after 0 to 2.5 min of irradiation. In the chromatogram of the C4 column attached to the mass spectrometer, *apo*CB5:CoSalen 1:5 was observed, though the peak became broader and less intense as irradiation time increased. However, in the deconvoluted spectrum signals for the complex:protein adduct were no longer observed, because the sample did not ionize anymore even after only 10 s of irradiation (*data not shown*), indicating that irradiation in the presence of PS and SA had a significant effect on the protein. Semi-native gel electrophoresis (Fig. S16B)

showed protein monomer, dimer, and trimer bands before irradiation. After only 5 seconds of irradiation, the bands faded, indicating an effect on the protein stability and a change in its charge upon irradiation in presence of PS and SA, which is in line with the mass spectrometry results. On denaturing SDS-PAGE (Fig. S16C) the protein before irradiation showed a monomer band, while after addition of PS and SA and 5 s irradiation, a ladder of multimers could be observed, revealing a cross-linking effect as was observed after dark incubation. In other words, 450 nm light irradiation in presence of PS and SA affects the protein charge and stability even after just 5 seconds of irradiation.

Overall, the visibility of the protein signals in mass spectrometry and gel electrophoresis decreased after light irradiation in the presence of PS and SA. To gain a better view of the photocatalytic multimerization process SEC-MALS was employed on *apo*CB5:CoSalen 1:5 alone and on *apo*CB5:CoSalen 1:5 in presence of PS and SA, either kept in the dark or irradiated for 0.5 min and 120 min (Fig. 12). Compared to *apo*CB5:CoSalen 1:5 without PS and SA, the sample kept in the dark with PS and SA contained a much smaller monomeric population, the population size of aggregates was increased. After irradiation of *apo*CB5:CoSalen 1:5 in the presence of PS and SA for 0.5 min or 120 min, the band of monomeric protein eluted slower as a consequence of an increase of the protein mass (see section 2.7). Furthermore, both after 0.5 min and 120 min the major multimer populations corresponded to dimers and trimers, while in samples kept in the dark a much more uniform distribution of population sizes was observed. Finally, CD was used to observe the secondary structure of the protein after photocatalysis (Fig. 13). PS and SA were removed from the sample before the CD measurements using a Corning concentrator with a 5 kDa molecular weight cut-off (MWCO). The observed CD spectrum after photocatalysis showed a loss of alpha-helical character, and an increase in unfolded character, while some beta-sheet character remains. The folding of the protein was affected by light irradiation, but not entirely lost. Both SEC-MALS and CD showed that while the exposure to light in presence of PS and SA had a significant and rapid effect on the protein (ESI-MS, gel electrophoresis), it nonetheless remained intact, soluble, and partially folded**.**

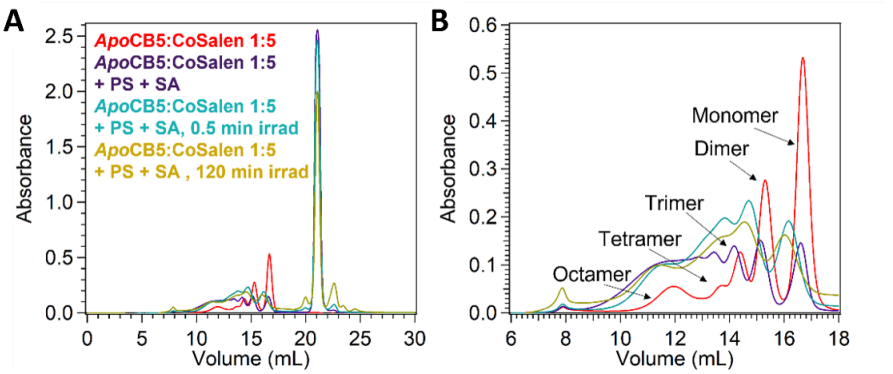

*Figure 12: UV-vis absorbance at 280 nm during SEC-MALS analysis of samples containing apoCB5:CoSalen 1:5 (50 µM) alone (red) and after combination with $[Ru(bpy)_3](ClO4)_2$ (0.3 mM) and $Na_2S_2O_8$ (5 mM) and either kept in the dark (purple), or irradiated for 0.5 min (blue) or 120 min (yellow) at 450 nm (18-19 mW) in the photoreactor setup (see supporting information for the detailed setup). Full chromatograms are shown in panel **A**. Panel **B** presents an enlarged view on the protein elution range with the aggregation state of each peak, determined from MALS (data not shown).*

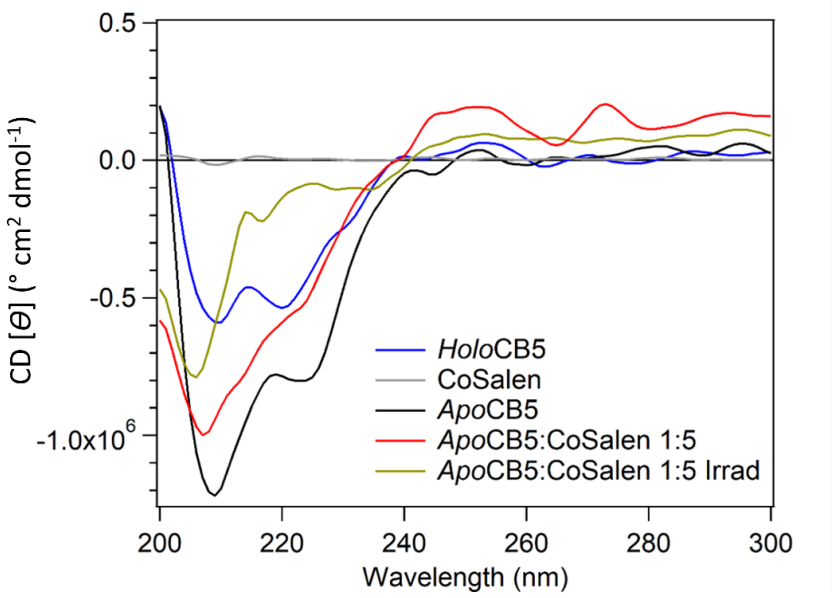

Figure 13: Circular dichroism (CD) analysis of apoCB5:CoSalen 1:5 (red), holoCB5 (blue), apoCB5 (black), free CoSalen (grey) and apoCB5:CoSalen 1:5

after irradiation in the presence of 0.3 mM $[Ru(bpy)_3](ClO_4)_2$ and 5 mM $Na_2S_2O_8$ after purification to remove small molecules (yellow).

2.7 Protein association with a breakdown product of the photosensitizer

While preparing light-irradiated samples for mass spectrometry, *via* purification over a P6 SEC column, visual changes to the eluate were observed, as it changed from virtually colourless before illumination to orange after irradiation for the samples of *apo*CB5:CoSalen 1:5 with PS and SA. We, therefore, suspected either aggregation of the orange, ruthenium containing, PS, or an association of the PS or a breakdown product thereof with protein. To investigate this phenomenon, ruthenium and cobalt concentration measurements by ICP-MS were recorded after purification of the sample over a microspin Bio-Rad P6 column with a 6 kDa MWCO that removed all small molecules, *i.e.*, excess of PS, SA. These measurements revealed that while the concentration of cobalt decreased from the *apo*CB5:CoSalen 1:5 sample during photocatalysis, the concentration of ruthenium increased considerably giving a CB5:ruthenium ratio of 1:1 after a short light irradiation period of 0.5 min. The presence of ruthenium in the microspin Bio-Rad P6-purified ICP-MS samples indicated that either a ruthenium-containing particle with a molecular weight larger than 6 kDa was formed during irradiation of *apo*CB5:CoSalen 1:5 in presence of PS and SA, or that there was an interaction between a ruthenium species and *apo*CB5.

A UV-vis spectrum was measured of the microspin Bio-Rad P6-purified sample to determine the spectral characteristics of this orange material. As shown in Fig. 14, an absorbance maximum around 450 nm was observed, which is characteristic for $[Ru(bpy)_3]^{2+}$. Since the orange material was observed after irradiation of the sample in presence of PS and SA and *apo*CB5:CoSalen 1:5 exposed to PS and SA in the dark is essentially colourless after purification, the bound ruthenium was hypothesized to be a breakdown product of the PS. To determine if the observed ruthenium species is an aggregate of photosensitizer-derived breakdown product, or if a breakdown product of the photosensitizer has indeed bound to the protein, SEC-MALS was used to monitor the co-elution of the protein and the ruthenium species (Fig. 15). This was done by monitoring the UV-vis absorbance of the sample during elution of the SEC column at 280 nm, where both the protein and the

ruthenium species absorb light, and at the 450 nm absorbance for the ruthenium species. The absorbance ratio A_{280}/A_{450} was determined for a solution of *apo*CB5:CoSalen 1:5, PS, and SA, at different time points of a photocatalytic dioxygen evolution experiment (t = 0, 0.5, 120 min, or in a dark control, Table S5). The dark *apo*CB5:CoSalen 1:5 sample containing PS and SA showed similar ratios compared to *apo*CB5:CoSalen 1:5 alone in solution, showing that no interaction of the protein and the ruthenium photosensitizer took place before irradiation. After 0.5 min of irradiation the A_{280}/A_{450} ratio decreased, which, in combination with the beforementioned ICP-MS results, indicated an increase in photosensitizer breakdown product concentration with respect to CB5. This spectral signature of the ruthenium compound was present with each multimer of the protein as it was eluted from the SEC column, indicating the ruthenium compound was indeed likely bound to the protein.

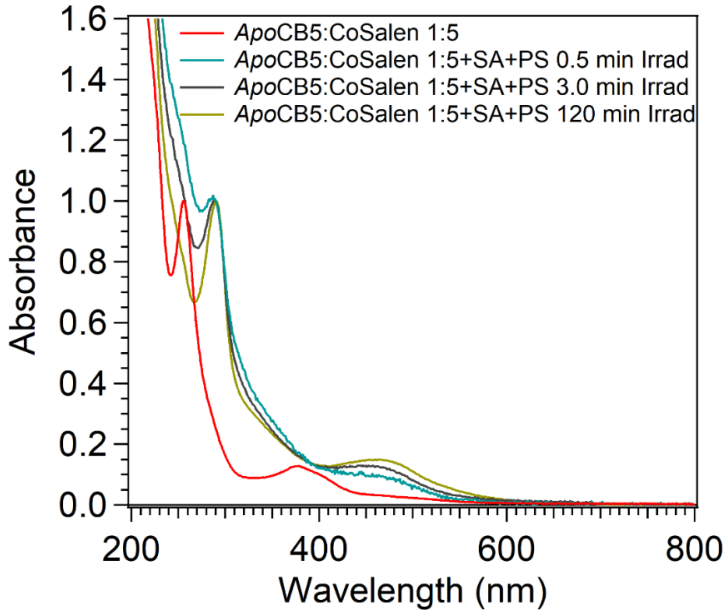

Figure 14: The stability of CB5:CoSalen 1:5 under photocatalytic conditions. Normalized (to the lambda max) UV-vis spectra measured after purification over a P6 column of apoCB5:CoSalen 1:5 samples kept in the dark (red), irradiated for 0.5 min (blue), 3 min (black), or 120 min (yellow) with a 450 nm LED (18-19mW) in the photoreactor in the presence of 0.3 mM $[Ru(bpy)_3(ClO_4)_2$ and 5 mM $Na_2S_2O_8$.

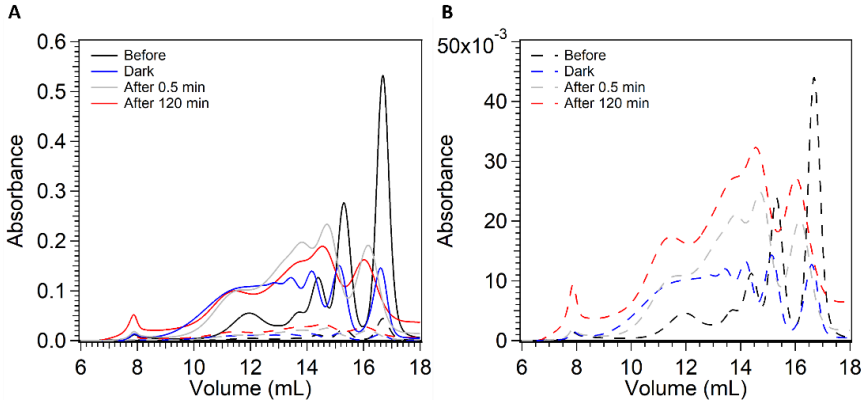

Figure 15: The 280 nm (solid lines) and 450 nm (broken lines) chromatograms of CB5:CoSalen 1:5 (black), CB5:CoSalen 1:5 kept dark in presence of 0.3 mM $[Ru(bpy)_3](ClO_4)_2$ and 5 mM $Na_2S_2O_8$ (blue), CB5:CoSalen 1:5 irradiated for 0.5 min in presence of 0.3 mM $[Ru(bpy)_3](ClO_4)_2$ and 5 mM $Na_2S_2O_8$ (grey), and CB5:CoSalen 1:5 irradiated for 120 min in presence of 0.3 mM $[Ru(bpy)_3](ClO_4)_2$ and 5 mM $Na_2S_2O_8$ (red).

3 DISCUSSION

In this study, we analysed one of the rare cases of light-induced generation of O_2 using an artificial metalloenzyme bearing an abundant metal cofactor. For most reported photoactive water oxidation systems using small-molecule cobalt catalysts, the instability or decomposition of the complex lead to the formation of cobalt nanoparticles or deposits [80–85]. By contrast, here we present a system in which nanoparticle formation is avoided.

For *apo*CB5:CoSalen 1:1, photocatalytic activity was not observed in the presence of PS, SA, and blue light. NMR data revealed that CoSalen was likely coordinated in the binding pocket of *apo*CB5 between two axial histidines, H44 and H68. This bi-coordination in the pocket of CB5 is different from what can be found in the literature for artificial haem proteins, where most of the cofactors are coordinated only by one residue in the pocket of the protein such that one coordination site on the metal is left open [86,87]. Bi-coordination leaves no free position on cobalt to coordinate water, while in some cases it is possible for redox reactions to take place on the ligands rather than at the metal centre [88–93], the coordination is likely the reason

why catalysis does not occur with *apo*CB5:CoSalen 1:1. Other potential explanations for the inactivity are that, while CB5 is a relatively small and open protein, either water or the excited photosensitizer could be restricted in its ability to approach the cobalt compound. In any case, the environment provided by the protein stabilized the complex in such a way that in our photocatalytic conditions no active cobalt species capable of water oxidation could be formed. By contrast, *apo*CB5:CoSalen 1:5 was found to be catalytically active. This may be explained by the following hypotheses: 1. A trend can be observed in which an increase in the protein concentration in the sample leads to a decrease in activity. The TON of the samples can be ordered as follows: Free CoSalen containing 0 µM CB5>*apo*CB5:CoSalen 1:5 containing ~13 µM CB5> *apo*CB5:CoSalen 1:1 contain ~50 µM CB5. Hypothesis 1: the presence of the protein inhibits the activity of CoSalen. 2. The *apo*CB5:CoSalen 1:1 sample in which CoSalen is bound in the binding pocket shows no activity, while the *apo*CB5:CoSalen 1:5 and *holo*CB5:CoSalen samples, in which CoSalen is also bound to the protein exterior, do show activity. Hypothesis 2: The exterior-bound CoSalen molecules determine whether or not the ArM is photocatalytically active.

Fitting hypothesis 1, indeed more protein seems to lead to less activity, one could imagine that the protein blocks the activity of CoSalen by preventing it from forming the active nanoparticle species. However, we do not have free CoSalen present in any sample, in each sample all CoSalen is bound to CB5 at the start of the experiment. Rather it seems more likely that the binding mode is the defining difference as in hypothesis 2. We also don't observe nanoparticles in any protein-containing samples regardless of if they were active. There is no gradual transition to a behaviour that is less and less like free CoSalen.

To further test hypothesis 2, we prepared *holo*CB5:CoSalen 1:5, where haem was still bound to the protein scaffold and the *holo*CB5:CoSalen binding ratio after purification was 1:2.7. The artificial *holo*CB5:CoSalen 1:5 system was photocatalytically active under the same conditions as *apo*CB5:CoSalen 1:5 but generated less O_2. This showed that the location where CoSalen is (originally) bound to the protein determined whether the sample was active. In contrast, purification of the sample after photocatalysis followed by ICP-MS revealed that CoSalen did not remain bound to the protein in its original form. DLS indicates no significant change in the size distribution of the

particles present in the photocatalytic solution of the *apo*CB5:CoSalen 1:5 sample, without any precipitation, unlike CoSalen in solution which forms nanoparticles (Fig. 10). The above showed that the artificial cobalt-protein is a pre-catalyst, like CoSalen, but unlike free CoSalen it forms a non-aggregated catalytically active species involving the protein upon exposure to light, the photosensitizer, and sodium persulfate (Fig. 16). In short: we hypothesize here that there is a dynamic interaction between cobalt and the protein, which generates an active, soluble adduct during photocatalysis, that is not stable enough to be detected afterwards, since the interaction between the catalytically active cobalt species and the protein did not survive a single passage through a microspin Bio-Rad P6 column.

The amount of O_2 produced by our most active system (*apo*CB5:CoSalen 1:5) was approximately 75% of what free CoSalen produced (Table S4). Considering that from 4 molecules of CoSalen bound *per apo*CB5 potentially only 3 are active, the activity of *apo*CB5:CoSalen 1:5 samples is comparable to free CoSalen in a homogeneous solution. The reduction of the amount of evolved O_2 in our systems, compared to free CoSalen, may have several other origins. One of them is the presence of haem in *holo*CB5:CoSalen 1:5 samples. It has been reported that Fe^{3+} from haem bound to proteins can be oxidized by the triplet excited state of $[Ru(bpy)_3]^{2+}$ generated during photocatalysis and that such a redox process is reversible and might lead to charge recombination [94,95]. Another reason can be found in the loss of the tryptophan fluorescence of the protein after irradiation in presence of PS and SA. This can be ascribed to the oxidation of tryptophan (as suggested by the fluorescence data in section 2.6), due to: a) the reaction of singlet oxygen generated by direct reaction of the triplet forming photosensitizer [96,97]; or b) the sulphate radical ($SO_4^{\bullet-}$) generated by 1-electron transfer from the excited state of the photosensitizer to sodium persulfate. $SO_4^{\bullet-}$ is a strong oxidant that might induce an electron transfer (ET) from the indole ring, leading to an oxidized, non-emissive aromatic moiety. These side reactions could lead to a reduction of activity in our protein-based systems.

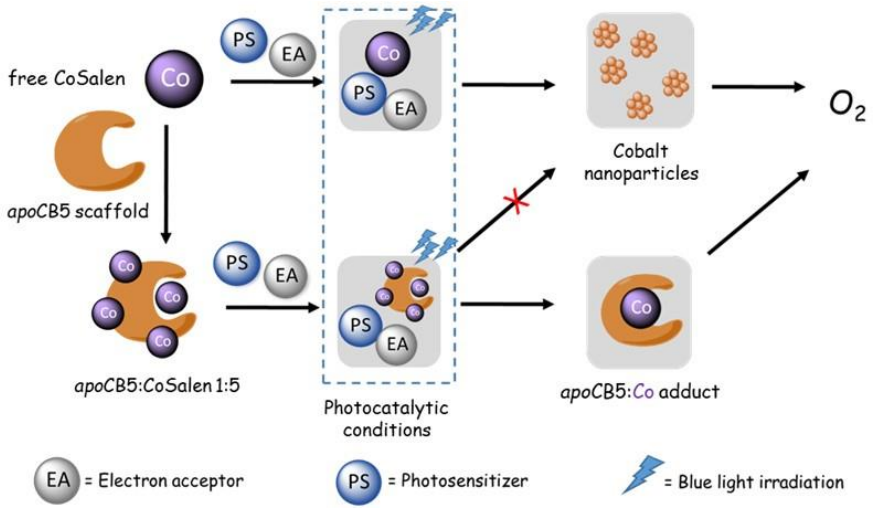

Figure 16: Proposed pathway of photocatalytic water oxidation using the apoCB5:CoSalen pre-catalyst compared to the free CoSalen pre-catalyst.

The presence of the above oxidizing species also has an effect on the protein scaffold. Analysis of the stability of *apo*CB5:CoSalen revealed that multimers/aggregates present in the PS- and SA-free sample become resistant to denaturation upon exposure to PS and SA in the dark as well as under irradiation (Fig. S15 and S16). It was hypothesized that such denaturation-resistant multimers are the result of a limited crosslinking of the protein as a consequence of the formation of tyrosine radicals, which shows that the protein scaffold experiences some degree of oxidation of its residues. Such oxidation of tyrosine leading to cross-linking after addition of PS and SA in the dark has been previously observed in literature [98,99]. Finally, a surprising result of irradiation of *apo*CB5:CoSalen 1:5 in presence of PS and SA was an interaction between the PS and the protein scaffold (section 2.7). The interaction was found to be in a 1:1 *apo*CB5:ruthenium ratio, in spite of the large, 6-fold, excess of PS, indicating some specificity of the binding. The interaction may be electrostatic in nature due to the positive charge of the PS, since *apo*CB5 has an overall negative charge, or dative due to ligand exchange of bipyridine under oxidative conditions with an amino acid, *e.g.,* histidine [12].

4 CONCLUSION

Here, novel artificial CB5:CoSalen metalloproteins, active for water oxidation under photocatalytic conditions, were developed and characterized. The system *apo*CB5:CoSalen 1:1, where CoSalen was bound *via* axial histidine coordination to the haem binding pocket of the protein, lacks catalytic activity. *Apo*CB5:CoSalen 1:5, in which CoSalen binds both in the binding pocket and to the exterior of the protein, showed water oxidation activity in photocatalytic conditions similar to free CoSalen. Slightly lower activity was observed from *holo*CB5:CoSalen 1:5, where CoSalen binds only the exterior of the protein. The presence of $[Ru(bpy)_3](ClO_4)_2$ and $Na_2S_2O_8$ led to limited protein crosslinking. Furthermore, one equivalent of the ruthenium photosensitizer was found to interact strongly with *apo*CB5:CoSalen 1:5 upon irradiation. During photocatalysis, the protein partially unfolded and protein-CoSalen interactions were destabilized. Strikingly, while the free CoSalen WOC formed nanoparticles capable of performing photocatalysis, no nanoparticles were found for the *apo*CB5:CoSalen 1:5 ArM that remained soluble. These results show the potential as well as the advantages of using a protein scaffold to act as support for an active molecule in harsh photocatalytic conditions. Overall, while this work is among the first studies of artificial proteins performing photocatalytic water oxidation, we conclude that using ArMs to achieve efficient photocatalytic water oxidation such as performed by the self-repairing Photosystem II, is still a daunting challenge.

5 REFERENCES

[1] D. J. Vinyard, G. M. Ananyev, and G. Charles Dismukes, “Photosystem II: the reaction center of oxygenic photosynthesis,” *Annual review of biochemistry*, vol. 82, pp. 577–606, 2013.

[2] W. Lubitz, E. J. Reijerse, and J. Messinger, “Solar water-splitting into H 2 and O 2: design principles of photosystem II and hydrogenases,” *Energy & Environmental Science*, vol. 1, no. 1, pp. 15–31, 2008.

[3] M. D. Karkas, O. Verho, E. V. Johnston, and B. Åkermark, “Artificial photosynthesis: molecular systems for catalytic water oxidation,” *Chemical reviews*, vol. 114, no. 24, pp. 11863–12001, 2014.

[4] C. Liu, D. van den Bos, B. den Hartog, D. van der Meij, A. Ramakrishnan, and S. Bonnet, “Ligand controls the activity of light-driven water oxidation catalyzed by nickel (II) porphyrin complexes in

neutral homogeneous aqueous solutions," *Angewandte Chemie International Edition*, vol. 60, no. 24, pp. 13463–13469, 2021.

[5] S. Ye, C. Ding, M. Liu, A. Wang, Q. Huang, and C. Li, "Water oxidation catalysts for artificial photosynthesis," *Advanced Materials*, vol. 31, no. 50, p. 1902069, 2019.

[6] R. Matheu *et al.*, "The development of molecular water oxidation catalysts," *Nature Reviews Chemistry*, vol. 3, no. 5, pp. 331–341, 2019.

[7] R. Matheu, M. Z. Ertem, C. Gimbert-Suriñach, X. Sala, and A. Llobet, "Seven coordinated molecular ruthenium–water oxidation catalysts: a coordination chemistry journey: focus review," *Chemical reviews*, vol. 119, no. 6, pp. 3453–3471, 2019.

[8] S. W. Gersten, G. J. Samuels, and T. J. Meyer, "Catalytic oxidation of water by an oxo-bridged ruthenium dimer," *Journal of the American Chemical Society*, vol. 104, no. 14, pp. 4029–4030, 1982.

[9] F. Liu, J. J. Concepcion, J. W. Jurss, T. Cardolaccia, J. L. Templeton, and T. J. Meyer, "Mechanisms of water oxidation from the blue dimer to photosystem II," *Inorganic Chemistry*, vol. 47, no. 6, pp. 1727–1752, 2008.

[10] J. K. Hurst, J. L. Cape, A. E. Clark, S. Das, and C. Qin, "Mechanisms of water oxidation catalyzed by ruthenium diimine complexes," *Inorganic chemistry*, vol. 47, no. 6, pp. 1753–1764, 2008.

[11] U. Hintermair, S. M. Hashmi, M. Elimelech, and R. H. Crabtree, "Particle formation during oxidation catalysis with Cp* iridium complexes," *Journal of the American Chemical Society*, vol. 134, no. 23, pp. 9785–9795, 2012.

[12] B. Limburg, E. Bouwman, and S. Bonnet, "Molecular water oxidation catalysts based on transition metals and their decomposition pathways," *Coordination Chemistry Reviews*, vol. 256, no. 15–16, pp. 1451–1467, 2012.

[13] T. Liu, B. Zhang, and L. Sun, "Iron-Based Molecular Water Oxidation Catalysts: Abundant, Cheap, and Promising," *Chemistry–An Asian Journal*, vol. 14, no. 1, pp. 31–43, 2019.

[14] S. C. Silver, J. Niklas, P. Du, O. G. Poluektov, D. M. Tiede, and L. M. Utschig, "Protein delivery of a Ni catalyst to photosystem I for light-driven hydrogen production," *Journal of the American Chemical Society*, vol. 135, no. 36, pp. 13246–13249, 2013.

[15] K. G. Kottrup, S. D'Agostini, P. H. van Langevelde, M. A. Siegler, and D. G. Hetterscheid, "Catalytic activity of an iron-based water oxidation catalyst: substrate effects of graphitic electrodes," *ACS catalysis*, vol. 8, no. 2, pp. 1052–1061, 2018.

[16] D. S. Nesterov and O. V. Nesterova, “Polynuclear cobalt complexes as catalysts for light-driven water oxidation: A review of recent advances,” *Catalysts*, vol. 8, no. 12, p. 602, 2018.

[17] B. Limburg, E. Bouwman, and S. Bonnet, “Rate and stability of photocatalytic water oxidation using [Ru (bpy) 3] 2+ as photosensitizer,” *ACS Catalysis*, vol. 6, no. 8, pp. 5273–5284, 2016.

[18] K. Degtyarenko, “Metalloproteins,” *Encyclopedia of Genetics, Genomics, Proteomics and Bioinformatics*, 2004.

[19] K. Vong, I. Nasibullin, and K. Tanaka, “Exploring and adapting the molecular selectivity of artificial metalloenzymes,” *Bulletin of the Chemical Society of Japan*, vol. 94, no. 2, pp. 382–396, 2021.

[20] K. Faber and K. Faber, *Biotransformations in organic chemistry: a textbook*, no. 660.634 F334B. Springer, 2004.

[21] K. Yamamura and E. T. Kaiser, “Studies on the oxidase activity of copper (II) carboxypeptidase A,” *Journal of the Chemical Society, Chemical Communications*, no. 20, pp. 830–831, 1976.

[22] M. E. Wilson and G. M. Whitesides, “Conversion of a protein to a homogeneous asymmetric hydrogenation catalyst by site-specific modification with a diphosphinerhodium (I) moiety,” *Journal of the American Chemical Society*, vol. 100, no. 1, pp. 306–307, 1978.

[23] F. Schwizer *et al.*, “Artificial metalloenzymes: reaction scope and optimization strategies,” *Chemical reviews*, vol. 118, no. 1, pp. 142–231, 2018.

[24] S. Lopez, L. Rondot, C. Leprêtre, C. Marchi-Delapierre, S. Menage, and C. Cavazza, “Cross-linked artificial enzyme crystals as heterogeneous catalysts for oxidation reactions,” *Journal of the American Chemical Society*, vol. 139, no. 49, pp. 17994–18002, 2017.

[25] Y. Yu, C. Hu, L. Xia, and J. Wang, “Artificial metalloenzyme design with unnatural amino acids and non-native cofactors,” *ACS Catalysis*, vol. 8, no. 3, pp. 1851–1863, 2018.

[26] H. M. Key, P. Dydio, D. S. Clark, and J. F. Hartwig, “Abiological catalysis by artificial haem proteins containing noble metals in place of iron,” *Nature*, vol. 534, no. 7608, pp. 534–537, 2016.

[27] J. Bos and G. Roelfes, “Artificial metalloenzymes for enantioselective catalysis,” *Current opinion in chemical biology*, vol. 19, pp. 135–143, 2014.

[28] K. Oohora, Y. Kihira, E. Mizohata, T. Inoue, and T. Hayashi, “C (sp3)–H bond hydroxylation catalyzed by myoglobin reconstituted with manganese porphycene,” *Journal of the American Chemical Society*, vol. 135, no. 46, pp. 17282–17285, 2013.

[29] S. Lopez *et al.*, “Efficient conversion of alkenes to chlorohydrins by a Ru-based artificial enzyme,” *Chemical Communications*, vol. 53, no. 25, pp. 3579–3582, 2017.

[30] I. Hamachi, S. Tanaka, and S. Shinkai, “Light-driven activation of reconstituted myoglobin with a ruthenium tris (2, 2’-bipyridine) pendant,” *Journal of the American Chemical Society*, vol. 115, no. 22, pp. 10458–10459, 1993.

[31] J. Liu *et al.*, “Metalloproteins containing cytochrome, iron–sulfur, or copper redox centers,” *Chemical reviews*, vol. 114, no. 8, pp. 4366–4469, 2014.

[32] S. N. Natoli and J. F. Hartwig, “Noble− metal substitution in hemoproteins: an emerging strategy for abiological catalysis,” *Accounts of chemical research*, vol. 52, no. 2, pp. 326–335, 2019.

[33] A. D. Liang, J. Serrano-Plana, R. L. Peterson, and T. R. Ward, “Artificial metalloenzymes based on the biotin–streptavidin technology: enzymatic cascades and directed evolution,” *Accounts of chemical research*, vol. 52, no. 3, pp. 585–595, 2019.

[34] N. J. Porter, E. Danelius, T. Gonen, and F. H. Arnold, “Biocatalytic carbene transfer using diazirines,” *Journal of the American Chemical Society*, vol. 144, no. 20, pp. 8892–8896, 2022.

[35] T. Lazarides *et al.*, “Visible light-driven O2 reduction by a porphyrin–laccase system,” *Journal of the American Chemical Society*, vol. 135, no. 8, pp. 3095–3103, 2013.

[36] V. Robert *et al.*, “Probing the Surface of a Laccase for Clues towards the Design of Chemo-Enzymatic Catalysts,” *ChemPlusChem*, vol. 82, no. 4, pp. 607–614, 2017.

[37] C. Esmieu, P. Raleiras, and G. Berggren, “From protein engineering to artificial enzymes–biological and biomimetic approaches towards sustainable hydrogen production,” *Sustainable Energy & Fuels*, vol. 2, no. 4, pp. 724–750, 2018.

[38] C. R. Schneider, A. C. Manesis, M. J. Stevenson, and H. S. Shafaat, “A photoactive semisynthetic metalloenzyme exhibits complete selectivity for CO 2 reduction in water,” *Chemical Communications*, vol. 54, no. 37, pp. 4681–4684, 2018.

[39] A. Pinnola, “The rise and fall of Light-Harvesting Complex Stress-Related proteins as photoprotection agents during evolution,” *Journal of Experimental Botany*, vol. 70, no. 20, pp. 5527–5535, 2019.

[40] R. E. Blankenship *et al.*, “Comparing photosynthetic and photovoltaic efficiencies and recognizing the potential for improvement,” *science*, vol. 332, no. 6031, pp. 805–809, 2011.

[41] P. Hosseinzadeh and Y. Lu, “Design and fine-tuning redox potentials of metalloproteins involved in electron transfer in bioenergetics,” *Biochimica et Biophysica Acta (BBA)-Bioenergetics*, vol. 1857, no. 5, pp. 557–581, 2016.

[42] P. K. Wawrzyniak, A. Alia, R. G. Schaap, M. M. Heemskerk, H. J. de Groot, and F. Buda, “Protein-induced geometric constraints and charge transfer in bacteriochlorophyll–histidine complexes in LH2,” *Physical Chemistry Chemical Physics*, vol. 10, no. 46, pp. 6971–6978, 2008.

[43] D. J. Sommer, M. D. Vaughn, and G. Ghirlanda, “Protein secondary-shell interactions enhance the photoinduced hydrogen production of cobalt protoporphyrin IX,” *Chemical communications*, vol. 50, no. 100, pp. 15852–15855, 2014.

[44] S. R. Soltau, P. D. Dahlberg, J. Niklas, O. G. Poluektov, K. L. Mulfort, and L. M. Utschig, “Ru–protein–Co biohybrids designed for solar hydrogen production: understanding electron transfer pathways related to photocatalytic function,” *Chemical Science*, vol. 7, no. 12, pp. 7068–7078, 2016.

[45] Z. Abdi, R. Bagheri, Z. Song, and M. M. Najafpour, “Water oxidation by ferritin: a semi-natural electrode,” *Scientific Reports*, vol. 9, no. 1, p. 11499, 2019.

[46] C. Casadevall, H. Zhang, S. Chen, D. J. Sommer, D.-K. Seo, and G. Ghirlanda, “Photoelectrochemical water oxidation by cobalt cytochrome c integrated-ato photoanode,” *Catalysts*, vol. 11, no. 5, p. 626, 2021.

[47] M. Kim and S. Lee, “Catalytic Water Oxidation by Iridium-Modified Carbonic Anhydrase,” *Chemistry–An Asian Journal*, vol. 13, no. 3, pp. 334–341, 2018.

[48] H. Ahmad, S. Kamarudin, L. J. Minggu, and M. Kassim, “Hydrogen from photo-catalytic water splitting process: A review,” *Renewable and Sustainable Energy Reviews*, vol. 43, pp. 599–610, 2015.

[49] B. You and Y. Sun, “Innovative strategies for electrocatalytic water splitting,” *Accounts of chemical research*, vol. 51, no. 7, pp. 1571–1580, 2018.

[50] J. Qi, W. Zhang, and R. Cao, “Solar-to-hydrogen energy conversion based on water splitting,” *Advanced Energy Materials*, vol. 8, no. 5, p. 1701620, 2018.

[51] M. Orio and D. A. Pantazis, “Successes, challenges, and opportunities for quantum chemistry in understanding metalloenzymes for solar

fuels research," *Chemical Communications*, vol. 57, no. 33, pp. 3952–3974, 2021.
[52] J. F. Allen and J. Nield, "Redox tuning in photosystem II," *Trends in Plant Science*, vol. 22, no. 2, pp. 97–99, 2017.
[53] V. M. Johnson and H. B. Pakrasi, "Advances in the Understanding of the Lifecycle of Photosystem II," *Microorganisms*, vol. 10, no. 5, p. 836, 2022.
[54] L. V. Opdam *et al.*, "A screening method for binding synthetic metallo-complexes to haem proteins," *Analytical Biochemistry*, vol. 653, p. 114788, 2022.
[55] E. Krieger and G. Vriend, "YASARA View—molecular graphics for all devices—from smartphones to workstations," *Bioinformatics*, vol. 30, no. 20, pp. 2981–2982, 2014.
[56] S. Bienert *et al.*, "The SWISS-MODEL Repository—new features and functionality," *Nucleic acids research*, vol. 45, no. D1, pp. D313–D319, 2017.
[57] N. Guex, M. C. Peitsch, and T. Schwede, "Automated comparative protein structure modeling with SWISS-MODEL and Swiss-PdbViewer: A historical perspective," *Electrophoresis*, vol. 30, no. S1, pp. S162–S173, 2009.
[58] A. Waterhouse *et al.*, "SWISS-MODEL: homology modelling of protein structures and complexes," *Nucleic acids research*, vol. 46, no. W1, pp. W296–W303, 2018.
[59] G. Studer, C. Rempfer, A. M. Waterhouse, R. Gumienny, J. Haas, and T. Schwede, "QMEANDisCo—distance constraints applied on model quality estimation," *Bioinformatics*, vol. 36, no. 6, pp. 1765–1771, 2020.
[60] M. Bertoni, F. Kiefer, M. Biasini, L. Bordoli, and T. Schwede, "Modeling protein quaternary structure of homo-and hetero-oligomers beyond binary interactions by homology," *Scientific reports*, vol. 7, no. 1, p. 10480, 2017.
[61] F. Teale, "Cleavage of the haem-protein link by acid methylethylketone," *Biochimica et biophysica acta*, vol. 35, p. 543, 1959.
[62] C. J. Falzone, Y. Wang, B. C. Vu, N. L. Scott, S. Bhattacharya, and J. T. Lecomte, "Structural and dynamic perturbations induced by heme binding in cytochrome b 5," *Biochemistry*, vol. 40, no. 15, pp. 4879–4891, 2001.

[63] N. J. Greenfield, “Using circular dichroism spectra to estimate protein secondary structure,” *Nature protocols*, vol. 1, no. 6, pp. 2876–2890, 2006.

[64] J. R. Lakowicz and J. R. Lakowicz, “Protein fluorescence,” *Principles of fluorescence spectroscopy*, pp. 445–486, 1999.

[65] Y. Chen and M. D. Barkley, “Toward understanding tryptophan fluorescence in proteins,” *Biochemistry*, vol. 37, no. 28, pp. 9976–9982, 1998.

[66] C. A. Royer, “Probing protein folding and conformational transitions with fluorescence,” *Chemical reviews*, vol. 106, no. 5, pp. 1769–1784, 2006.

[67] M. M. Lee and B. R. Peterson, “Quantification of small molecule–protein interactions using FRET between tryptophan and the pacific blue fluorophore,” *ACS omega*, vol. 1, no. 6, pp. 1266–1276, 2016.

[68] K. D. Bhatt, H. S. Gupte, B. A. Makwana, D. J. Vyas, D. Maity, and V. K. Jain, “Calix receptor edifice; scrupulous turn off fluorescent sensor for Fe (III), Co (II) and Cu (II),” *Journal of fluorescence*, vol. 22, pp. 1493–1500, 2012.

[69] L. Fabbrizzi, M. Licchelli, P. Pallavicini, D. Sacchi, and A. Taglietti, “Sensing of transition metals through fluorescence quenching or enhancement. A review,” *Analyst*, vol. 121, no. 12, pp. 1763–1768, 1996.

[70] Y. Li, Z. Csók, P. Szuroczki, L. Kollár, L. Kiss, and S. Kunsági-Máté, “Fluorescence quenching studies on the interaction of a novel deepened cavitand towards some transition metal ions,” *Analytica Chimica Acta*, vol. 799, pp. 51–56, 2013.

[71] Y. Chang, Z. Zhang, H. Liu, N. Wang, and J. Tang, “Cobalt oxyhydroxide nanoflake based fluorescence sensing platform for label-free detection of DNA,” *Analyst*, vol. 141, no. 15, pp. 4719–4724, 2016.

[72] D. Kong, F. Yan, Z. Han, J. Xu, X. Guo, and L. Chen, “Cobalt (II) ions detection using carbon dots as an sensitive and selective fluorescent probe,” *RSC advances*, vol. 6, no. 72, pp. 67481–67487, 2016.

[73] E. B. Azimi, A. Badiei, M. Jafari, A. B. Dehkordi, J. B. Ghasemi, and G. M. Ziarani, “Boron-doped graphitic carbon nitride as a novel fluorescent probe for mercury (II) and iron (III): A circuit logic gate mimic,” *New Journal of Chemistry*, vol. 43, no. 30, pp. 12087–12093, 2019.

[74] W. Boonta *et al.*, “The synthesis of nitrogen and sulfur co-doped graphene quantum dots for fluorescence detection of cobalt (II) ions

in water," *Materials Chemistry Frontiers*, vol. 4, no. 2, pp. 507–516, 2020.
[75] L. D. Newton, S. I. Pascu, R. M. Tyrrell, and I. M. Eggleston, "Development of a peptide-based fluorescent probe for biological heme monitoring," *Organic & Biomolecular Chemistry*, vol. 17, no. 3, pp. 467–471, 2019.
[76] S. Koga *et al.*, "Development of a heme sensor using fluorescently labeled heme oxygenase-1," *Analytical biochemistry*, vol. 433, no. 1, pp. 2–9, 2013.
[77] B. Bennett, "EPR of cobalt-substituted zinc enzymes," in *Metals in Biology: Applications of High-Resolution EPR to Metalloenzymes*, Springer, 2009, pp. 345–370.
[78] J. Zarembowitch and O. Kahn, "Magnetic properties of some spin-crossover, high-spin, and low-spin cobalt (II) complexes with Schiff bases derived from 3-formylsalicylic acid," *Inorganic Chemistry*, vol. 23, no. 5, pp. 589–593, 1984.
[79] M. C. Symons, T. Taiwo, A. M. Sargeson, M. M. Ali, and A. S. Tabl, "EPR spectra for high-and low-spin CoII encapsulated complexes," *Inorganica chimica acta*, vol. 241, no. 2, pp. 5–8, 1996.
[80] S. Fu *et al.*, "A mononuclear cobalt complex with an organic ligand acting as a precatalyst for efficient visible light-driven water oxidation," *Chemical communications*, vol. 50, no. 17, pp. 2167–2169, 2014.
[81] D. den Boer *et al.*, "On the homogeneity of a cobalt-based water oxidation catalyst," *ACS catalysis*, vol. 12, no. 8, pp. 4597–4607, 2022.
[82] D. Hong *et al.*, "Water-soluble mononuclear cobalt complexes with organic ligands acting as precatalysts for efficient photocatalytic water oxidation," *Energy & Environmental Science*, vol. 5, no. 6, pp. 7606–7616, 2012.
[83] M. Risch *et al.*, "Atomic structure of cobalt-oxide nanoparticles active in light-driven catalysis of water oxidation," *International journal of hydrogen energy*, vol. 37, no. 10, pp. 8878–8888, 2012.
[84] M. W. Kanan and D. G. Nocera, "In situ formation of an oxygen-evolving catalyst in neutral water containing phosphate and Co2+," *Science*, vol. 321, no. 5892, pp. 1072–1075, 2008.
[85] D. Shevchenko, M. F. Anderlund, A. Thapper, and S. Styring, "Photochemical water oxidation with visible light using a cobalt containing catalyst," *Energy & Environmental Science*, vol. 4, no. 4, pp. 1284–1287, 2011.

[86] K. Oohora and T. Hayashi, “Myoglobins engineered with artificial cofactors serve as artificial metalloenzymes and models of natural enzymes,” *Dalton Transactions*, vol. 50, no. 6, pp. 1940–1949, 2021.
[87] Y. Miyazaki, K. Oohora, and T. Hayashi, “Methane generation via intraprotein C–S bond cleavage in cytochrome b562 reconstituted with nickel didehydrocorrin,” *Journal of Organometallic Chemistry*, vol. 901, p. 120945, 2019.
[88] H. M. Castro-Cruz and N. A. Macias-Ruvalcaba, “Porphyrin-catalyzed electrochemical hydrogen evolution reaction. Metal-centered and ligand-centered mechanisms,” *Coordination Chemistry Reviews*, vol. 458, p. 214430, 2022.
[89] O. R. Luca and R. H. Crabtree, “Redox-active ligands in catalysis,” *Chemical Society Reviews*, vol. 42, no. 4, pp. 1440–1459, 2013.
[90] J. I. van der Vlugt, “Cooperative catalysis with first-row late transition metals,” *European Journal of Inorganic Chemistry*, vol. 2012, no. 3, pp. 363–375, 2012.
[91] V. Lyaskovskyy and B. de Bruin, “Redox non-innocent ligands: versatile new tools to control catalytic reactions,” *Acs Catalysis*, vol. 2, no. 2, pp. 270–279, 2012.
[92] D. J. Sommer, M. D. Vaughn, B. C. Clark, J. Tomlin, A. Roy, and G. Ghirlanda, “Reengineering cyt b562 for hydrogen production: A facile route to artificial hydrogenases,” *Biochimica et Biophysica Acta (BBA)-Bioenergetics*, vol. 1857, no. 5, pp. 598–603, 2016.
[93] S. Salzl, M. Ertl, and G. Knör, “Evidence for photosensitised hydrogen production from water in the absence of precious metals, redox-mediators and co-catalysts,” *Physical Chemistry Chemical Physics*, vol. 19, no. 12, pp. 8141–8147, 2017.
[94] J. Chen and W. R. Browne, “Photochemistry of iron complexes,” *Coordination Chemistry Reviews*, vol. 374, pp. 15–35, 2018.
[95] J. R. Scott *et al.*, “Intramolecular electron transfer in cytochrome b5 labeled with ruthenium (II) polypyridine complexes: rate measurements in the Marcus inverted region,” *Journal of the American Chemical Society*, vol. 115, no. 15, pp. 6820–6824, 1993.
[96] G. E. Ronsein, M. C. Oliveira, S. Miyamoto, M. H. Medeiros, and P. Di Mascio, “Tryptophan oxidation by singlet molecular oxygen [O2 (1Δg)]: mechanistic studies using 18O-labeled hydroperoxides, mass spectrometry, and light emission measurements,” *Chemical research in toxicology*, vol. 21, no. 6, pp. 1271–1283, 2008.
[97] M. Ehrenshaft, L. J. Deterding, and R. P. Mason, “Tripping up Trp: Modification of protein tryptophan residues by reactive oxygen

species, modes of detection, and biological consequences," *Free Radical Biology and Medicine*, vol. 89, pp. 220–228, 2015.

[98] B. G. Soliman *et al.*, "Stepwise control of crosslinking in a one-pot system for bioprinting of low-density bioinks," *Advanced Healthcare Materials*, vol. 9, no. 15, p. 1901544, 2020.

[99] J. W. Bjork, S. L. Johnson, and R. T. Tranquillo, "Ruthenium-catalyzed photo cross-linking of fibrin-based engineered tissue," *Biomaterials*, vol. 32, no. 10, pp. 2479–2488, 2011.

6 SUPPORTING INFORMATION

6.1 Supplementary A: Materials

All chemicals were of analytical grade and were purchased from Sigma Aldrich (Missouri USA) unless stated otherwise. $[Ru(bpy)_3](ClO_4)_2$ was synthesized following the reported procedure [1]. Complex N,N'-Bis(salicylidene)ethylenediaminocobalt (II) (catalyst CoSalen) was purchased from Alfa Aesar (Massachusetts, USA). Purified water was obtained using a Milli-Q system (Advantage A10, Merck MilliporeSigma, Jersey USA).

6.2 Supplementary B: Methods and techniques

Liquid chromatography-mass spectrometry (LC-MS) was conducted on a Finnigan LCQ Advantage MAX apparatus (Thermo Fisher Scientific, Massachusetts, USA) with a Gemini 3 µm NX-C18 column (Phenomenex, California USA), using a gradient of 10% MeCN in H_2O to 90% MeCN in H_2O with 0.1% TFA as eluent.

High resolution-mass spectrometry (HR-MS) was performed in a Thermo Scientific Q Exactive Orbitrap (ESI+) (Massachusetts, USA) coupled to an Ultimate 3000 nanosystem (3,5 kV; 275 °C; Resolution R=240.000 at *m/z*=400; external lock; mass range *m/z*=150-1500) (Thermo Fisher Scientific, Massachusetts, USA). Mobile phase MeCN/H_2O (1:1 *v*/*v*) with 0.1% formic acid, flow= 25 µL/min, direct injection of a 1 µM sample.

Electrospray ionization-mass spectrometry (ESI-MS) was performed with a Synapt G2-Si mass spectrometer from Waters (Massachusetts, USA). Initial separation and denaturing of protein samples was achieved using a nanoEase *M/Z* protein BEH reverse phase C4 column, 300 Å, 1.7 µM x 50 mm, 1/pk (Waters, Massachusetts, USA). Samples were prepared in 10 mM NH_4Ac buffer at pH 7.0 using a Micro Bio-Spin P6 gel desalting column from Bio-Rad (California, USA), maximally 30 min before being run. Deconvolution was performed using the MaxEnt. algorithm of the MassLynx software version 4.2.

UV-vis was measured with an Agilent Cary60 UV-vis spectrophotometer (California, USA) using a quartz cuvette having a 1 cm optical path length. For irradiation experiments followed by UV-vis a 450 nm LED was used as depicted in Fig. S1. The power intensity of the LED was set between 19-20

mW using a current of 350 mA, the sample volume was 3 mL, all samples were degassed with Ar for 30 min prior to irradiation and all experiments were performed under constant stirring. A spectrum recorded at *t* = 0 min, *i.e.*, before irradiation, was used as a reference spectrum.

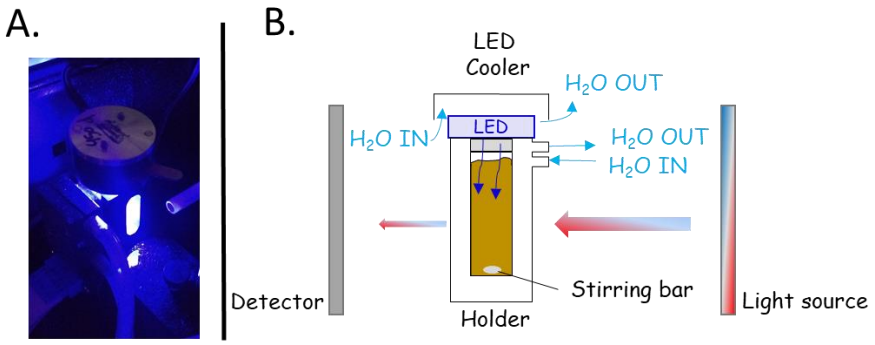

*Figure S1: . Irradiation setup for following UV-vis with an integrated cooling system set at 25 °C. Irradiation setup with 450 nm LED in the UV-vis holder (**A**). Scheme of setup of UV-vis cuvette for irradiation of a sample (**B**).*

Circular Dichroism (CD) data were recorded with a BioLogic (Tennessee, USA) MOS-500 spectropolarimeter on a 700 µL sample in a 0.2 cm quartz cuvette. A Bio-Logic (Tennessee, USA) SAS lightbox with a Xe lamp as a light source was used. An ALX300 power supply was used and always set to 150 W. Data were obtained and processed using Biokine software.

Dynamic light scattering (DLS) measurements were performed with a DynaPro NANOSTAR device from Wyatt technology (Santa Barbara, USA) using a 5 µL cuvette. Data were recorded and processed using the Dynamics 7.10.1.21 software.

Steady-state fluorescence measurements were performed with an F929 Fluorescence spectrometer from Edinburg instruments (Livingston, UK) using a Xe900 lamp as a light source and an R928P emission detector. Data were recorded and processed using the FS900 software.

For Inductively coupled plasma-mass spectrometry (ICP-MS), the samples were prepared by diluting 20-30 µL of the sample to 200 µL with MilliQ water. Then, concentrated nitric acid (400 µL, 65%) was added to each sample, and the samples were digested overnight in the oven in glass test tubes at 90 °C

with a glass marble on top. Then 2.4 mL MilliQ water was added to each sample. Afterwards, 1 mL of each sample was diluted with 9 mL of MilliQ water, to reach a total volume of 10 mL (HNO_3 concentration 2.2%). The cobalt and ruthenium concentration of each sample was subsequently measured in triplicate using a NexION 2000 ICP mass spectrometer, an SC2 DX autosampler, and Syngistix software from Perkin Elmer (Massachusetts, USA).

Size exclusion chromatography multi-angle light scattering (SEC-MALS) measurements were performed on a miniDAWN analytical HPLC/FPLC from Wyatt technology (Santa Barbara, USA) using a Superdex 200 Increase 10/300 GL SEC column with eluent 80 mM NaPi + 100 mM NaCl pH 7.5. Data were analysed using the Astra software.

Homology models of *apo*- and *holo*CB5 were generated using Swiss model [2–6]. The model of *apo*CB5 is based on the structure of *Rattus norvegicus apo*CB5 from PDB-ID 1IEU [7] with which it shares 81% sequence identity. The model of truncated *holo*CB5 was based on *Sus scrofa* CB5 from PDB-ID 3X33,[8] with which it shared 97% sequence identity.

Nuclear magnetic resonance (NMR) spectroscopy was measured with a Bruker (Rheinstetten, Germany) AVIII HD 850 MHz (20.0 T) with a TCI cryoprobe. The samples were prepared from protein expressed in ^{15}N-labelled M9 minimal medium with additional iron so that the total amount is 0.6 g/50 mL in the 10x trace element solution, purified and prepared in the *apo*-state as detailed below, and finally buffer exchanged to a 20 mM NaPi buffer at pH 7.5 unless otherwise specified, 6% D_2O was added. All experiments were performed at 293 K, in all spectra the zgpr program for water-suppression was used. Large window HSQC spectra were performed with a cnst 4 set to 7 Hz and the receiver gain was kept at 912. Normal HSQC spectra were performed using the hsqcf3gpph19 pulse program.

For Electron paramagnetic resonance (EPR) analysis, samples containing the solution to analyse were transferred into 4 mm outer diameter EPR quartz tubes and frozen in liquid nitrogen. Continuous wave EPR at X Band (9.5 GHz)

was performed on a Bruker Elxsys E680 (Bruker, Rheinstetten, Germany) spectrometer equipped with a TE_{102} cavity and an ESR900 Cryostat (Oxford Instrument, Abingdon, UK). Low temperature was achieved with a constant

helium flow. Parameters were the following: modulation amplitude 1 mT, modulation frequency 100 kHz, microwave power 20 mW, total measurement time of 1 h, and measurement temperature 10 K. Simulations were performed on MatLab using Easyspin version 5.2.33 [9].

Simulation of the EPR spectrum of CoSalen in buffer was performed with a **g** tensor of $\mathbf{g} = [g_{xx}\ g_{yy}\ g_{zz}] = [5.27\ 3.85\ 2.22]$. As line broadening an H-strain was used with the components 3499 MHz, 5235 MHz, and 2896 MHz in the respective **g** tensor directions. Simulation of the spectrum of CoSalen in chloroform was performed with an axial g tensor of $g_{xx} = g_{yy} = 2.023$, $g_{zz} = 3.11$ and a hyperfine splitting due to coupling with the $I = 7/2$ ^{59}Co nucleus of A_{zz} = 398 MHz, which can be seen as eight lines at 230 mT (g_{zz} direction). As line broadening a **g**-strain was used equal to 0.03 for each one of the **g** tensor directions.

(Semi-native) Gel electrophoresis was performed using 15% polyacrylamide gels containing 0.1% sodium dodecyl sulphate (SDS). Cracking buffer for semi-native PAGE was prepared in absence of SDS and β-mercaptoethanol. The gels were run on a Mini-Protean System and PowerPac Basic Power Supply from Bio-Rad (California, USA) for 50 min at 200 V. The gels were imaged with 2,2,2-trichloroethanol (5 µL per mL was added to the gel mixture, Sigma Aldrich) or coomassie brilliant blue (gels were fixed prior to staining) as specified with each Fig., using a Gel Doc XR+ from Bio-Rad. Gel images were processed using the Image Lab Software version 6.01 from Bio-Rad, adjusting the gamma setting to improve the contrast.

For water oxidation, the setup used was as shown in Fig. S2. A 3.5mL solution in phosphate buffer 80 mM, pH 7.5 containing the adduct CB5:CoSalen, the photosensitizer $[Ru(bpy)_3](ClO_4)_2$, and the sacrificial electron acceptor $Na_2S_2O_8$, were placed in a 3.5 mL inner volume photoreactor with an integrated water-cooling system settled at 25 ^{o}C. Every sample was degassed for 30 min with Ar directly in the reactor and then recorded for 30 min in the dark before irradiation started. 700 rpm stirring speed was set for the reaction. An Unisense (Aarhus, Denmark) Clark electrode needle type sensor (Unisense OX-NP) controlled by an x-5 UniAmp with Logger software was used for measuring the dioxygen concentration in real time. The sensor was calibrated using a pure O_2 as reference which allowed the building of a calibration curve. The sensor was fixed using a rubber septum and two silicon

septa to avoid air leakage as much as possible. O_2 evolution was measured in the gas phase where the tip of the sensor was placed. As an irradiation source, OSRAM Opto semiconductors (Regensburg, Germany) 450 nm LEDs were used. Light power was measured before and after every irradiation to ensure the stability of the light with an OPHIR (Jerusalem, Israel) Nova-Display laser power meter. Standard ferrioxilate actinometry of each LED was performed to determine the photon flux Φ (mol s^{-1}) using a power source of 350 mA: 450e = 9.41E-08 mol s^{-1} (19 mW); 450f =1.12E-07 mol s^{-1} (19 mW); 450g =1.03E-07 mol s^{-1} (19 mW).

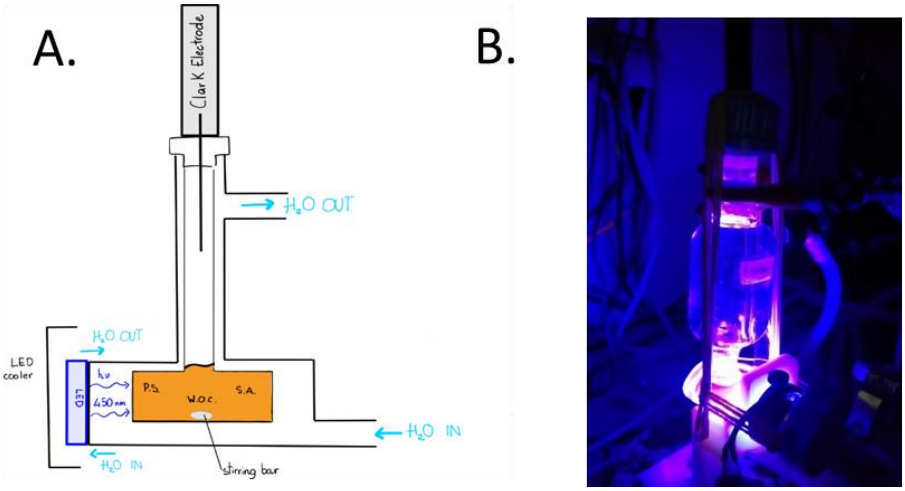

*Figure S2: Water oxidation setup. Integrated cooling system set at 25 °C. Oxygen evolution in the gas phase was detected using a Clark Electrode; the photocatalytic system was closed using hermetic septa on the top to avoid air leakage. Scheme of the irradiation setup for O_2 detection during photocatalytic water oxidation (**A**). Photograph of the photoreactor setup while irradiating at 450 nm (**B**).*

6.2.1 *TON*, *TOF* and O_2 quantum yield determination

The turnover number (*TON*) was calculated using Equation S1, where η_{O2} (µmol) is the number of mol of dioxygen produced by the system during an irradiation period of 120 min; η_{CAT} (µmol) is the number of mol of catalyst used in the photocatalytic system.

$$TON = \frac{\eta_{O2}}{\eta_{CAT}} \qquad \text{S1}$$

The O_2 production quantum yield (φ) was calculated according to Equation S2 as reported in the literature:[2]

$$\varphi = \frac{2\eta_{CAT} TOF_{max}}{60\,\Phi(1\text{-}10^{-A_e})(\frac{A_{PS}}{A_e})} \quad \text{S2}$$

where η_{CAT} (µmol) is the number of mol of catalyst used in the photocatalytic system, Φ (µmol s^{-1}) is the photon flux determined by standard ferrioxilate actinometry, A_e is the total absorption of the sample at the irradiation wavelength (here 450 nm), A_{PS} is the absorbance at 450 nm due to the PS only, TOF_{max} is the maximum turnover frequency which is calculated according to the literature [10].

6.2.2 Protein expression and purification

The plasmid for expression of CB5 was kindly provided by the laboratory of Prof. Marcellus Ubbink. CB5 was expressed in *Escherichia coli* BL21 PLysS and purified as detailed in Chapter 2.

Site directed mutagenesis was performed to introduce the H20Y, H31Y, and H85Y mutations *via* the WholePlasmid Synthesis (WOPS) protocol [11], using the primers found in the table below. The primers were obtained from Sigma-Aldrich (Missouri, USA), and the *Pfu* polymerase was produced in-house. The correct incorporation of the mutations was checked using Sanger sequencing data (Baseclear BV, Leiden, The Netherlands).

Mutation	5' Mod	Sequence	3' Mod
H20Y	CCC TGG AAG AAA TTC AAA AAT ACA ATA ACT CTA AAT CTA CCT GGC	T L E E I Q K Y N N S K S T	GCC AGG TAG ATT TAG AGT TAT TGT ATT TTT GAA TTT CTT CCA GGG
H31Y	CCT GGC TGA TCC TGT ATT ATA AAG TGT ACG ATC TGA CC	T W L I L Y Y K V Y D L T	GGT CAG ATC GTA CAC TTT ATA ATA CAG GAT CAG CCA GG
H85Y	GCA AAA CCT TTA TCA TTG GCG AAC TGT ACC CGG ACG ACC GTT AAC TCG	S K T F I I G E L Y P D D R - L	CGA GTT AAC GGT CGT CCG GGT ACA GTT CGC CAA TGA TAA AGG TTT TGC

6.2.3 Teale's method to prepare *apo*CB5

Haem was removed from cytochrome b_5 using Teale's method [12]. The pH of the protein sample was lowered to 2.0 by dropwise addition of 0.5 M HCl under constant stirring on ice. An equal volume of ice-cold 2-butanone was added and mixed, then pipetted off after the layers had separated, and this procedure was repeated 2-3 times until a colourless aqueous solution was obtained. The aqueous layer was pipetted directly into a 3.5 kDa cut-off dialysis bag (cellulose dialysis tubing from Spectrum Chemical, California, USA) and dialyzed against 2 L of 20 mM sodium phosphate buffer solution at pH 7.5 at 4 °C overnight. The dialysis buffer was exchanged once after 120 min of dialysis. To improve sample stability traces of 2-butanone were removed using 2 stacked 5 mL HiTrap desalting columns from Sigma Aldrich (Missouri, USA) to exchange to 20 mM NaPi pH 8.0. UV-vis was used to verify that the protein was in the *apo*state. *Apo*CB5 was re-concentrated and stored frozen (with liquid N_2) at -80 °C until use.

6.2.4 Protein-catalyst complex preparation

For the preparation of *apo*CB5:CoSalen 1:1 and *apo*CB5:CoSalen 1:5, *apo*CB5 from concentrated stock was reacted with CoSalen from a 4 mM stock in DMF (note that for NMR a 1 mM stock in milliQ was used) in respectively a 1:1 and 1:5 molar ratio, the final protein concentration during the reaction was 20 µM (so that the CoSalen concentrations were 20 µM or 100 µM, respectively). For the preparation of *holo*CB5:CoSalen, *holo*CB5 was reacted with CoSalen in a 1:5 molar ratio under the same conditions. The reactions were performed at 4 °C, overnight, on a Stuart STR9 roller from Sigma Aldrich (Missouri, USA) at 33 rpm. The resulting sample was concentrated to < 2 mL using a 20 mL, 5.000 kDa cut-off concentrator (Corning, New York, USA). DMF and excess CoSalen were removed using 2 stacked 5 mL HiTrap desalting columns from Sigma Aldrich (Missouri, USA) to exchange to 80 mM NaPi pH 7.5. The resulting sample was re-concentrated to < 2 mL using a 20 mL, 5.000 kDa cut-off concentrator (Corning, New York, USA). The concentration of protein was determined using a BCA protein assay kit from Bio-Rad (California, USA). The CoSalen concentrations were determined using ICP-MS as detailed above. The samples were finally stored frozen (with liquid N_2) at -80 °C until use.

For HR-MS measurements, samples containing only the protein were placed in a UV-vis cuvette and irradiated during a period of 160 min (see Fig. S1 for setup). A high-resolution spectrogram of each sample was measured following irradiation.

6.2.5 Water oxidation measurements

For every dataset in Fig. S8, the black line represents the average of the 2 measurements. The coloured traces represent the SD of all the measurements done for each set of data. All photocatalysis was carried on in degassed phosphate buffer pH 7.5, 80 mM, containing 50 µM of the catalyst (CoSalen or CoSalen-protein adduct), 0.3 mM of $[Ru(bpy)_3](ClO_4)_2$ and 5 mM of $Na_2S_2O_8$. The 450 nm LED-based light source was set at an intensity of 350 mA, which provided an optical power of 18-19 mW measured with an OPHIR (Jerusalem, Israel) Nova-Display laser power meter as mentioned. Data processing was performed according to the literature [10]. The average curve of each set of data was plotted using Origin 9.1 using the following method: Select a set of values →Statistics → descriptic statistics → statistics on Row → Compute Mean. Using the same software, the error was plotted using 5% of SD and then corrected with the next script: Statistics -> descriptic statistics -> statistics on Row -> Compute SD. All the O_2 evolution data were fitted using Origin 9.1 using the following method: Analysis-> Fitting -> Non-linear curve -> Growth/Sigmoidal category -> Hill1 function. The Hill1 function is described by equation S3:

$$y = \mathrm{START} + (\mathrm{END} - \mathrm{START})\frac{x^n}{(k^n + x^n)} \qquad \text{S3}$$

6.3 Supplementary C: Supplementary tables

Table S1. Stability of apoCB5:CoSalen 1:5 monitored by the protein:cobalt ratio determined after repeated purification over P6 spin columns.

***apo*CB5:CoSalen 1:5**	**Ratio [Co] / [*apo*CB5] (sDev)**
Purified 1x*	3.71 (0.14)
Purified 2x	3.69 (0.21)
Purified 3x	3.97 (0.15)

*Was purified by desalting column

Table S2. Assignment of histidine side chain nitrogen chemical shifts (see Fig. 6C for ring labelling) from LSW HSQC NMR spectra of apoCB5 (top), apoCB5:CoSalen 1:1 (middle), and apoCB5CoSalen 1:5 (bottom).

Sample	Assignment	Chemical shift ^{15}N (ppm)
*Apo*CB5	H85 Nε2	164.67
	H31 Nε2	178.23
	H44/68 Nε2	177.98
	H44/68 Nε2	180.43
	H44/68 Nδ1	212.79
*Apo*CB5: CoSalen 1:1	H85 Nε2	164.67
	H31 Nε2	177.49
	H44/68 Nε2	178.35
	H44/68 Nε2	161.50
	H44/68 Nε2	180.55
	H44/68 Nε2	166.14
*Apo*CB5: CoSalen 1:5	H85 Nε2	164.67
	H31 Nε2	161.62
	H31 Nδ1	174.32
	H44/68 Nε2	162.59
	H44/68 Nδ1	173.95
	H44/68 Nε2	166.38
	H44/68 Nδ1	~174

Table S3. Assignment of histidine side chain proton chemical shifts (see Fig. 6C for ring labelling) from LSW HSQC NMR spectra of apoCB5 (top), apoCB5:CoSalen 1:1 (middle) and apoCB5:CoSalen 1:5 (bottom).

Sample	Assignment	Chemical shift ^{1}H (ppm)
*Apo*CB5	H85 Hδ2	6.86
	H85 Hε1	7.39
	H31 Hδ2	6.72
	H31 Hε1	7.67
	H44/68 Hδ2	6.93
	H44/68 Hε1	7.76
	H44/68 Hδ2	6.89
	H44/68 Hε1	7.78
*Apo*CB5: CoSalen 1:1	H85 Hδ2	6.86
	H85 Hε1	7.39
	H31 Hδ2	6.74
	H44/68 Hδ2	6.93
	H44/68 Hδ2	6.24
	H44/68 Hδ2	6.89
	H44/68 Hδ2	6.19
*Apo*CB5: CoSalen 1:5	H85 Hδ2	6.86
	H85 Hε1	7.39
	H31 Hδ2	6.39
	H44/68 Hδ2	6.25
	H44/68 Hδ2	6.19

Table S4. The photoactivity of CoSalen in different systems

Sample	O_2 produced	*TON* [a]	TOF_{Max} [b]	φ_{O2} [c]
***apo*CB5**	-	-	-	-
Free CoSalen	5.57±0.85	31.80±4.83	1.36± 0.03	0.073± 0.001
***apo*CB5:CoSalen 1:1**	-	-	-	-
***apo*CB5:CoSalen 1:5**	4.24 ±0.24	24.25±1.35	0.63± 0.07	0.036± 0.004
***holo*CB5:CoSalen 1:5**	2.72 ±0.15	15.54±0.84	0.55± 0.09	0.032± 0.004

Conditions: PS = 0.3 mM $[Ru(bpy)_3](ClO_4)_2$, SA = 5 mM $Na_2S_2O_8$, [Cat] = 50 µM in Co, LED = 450 nm, 18-19 mW, 25 °C, 3.5 mL, 80 mM NaPi pH 7.5; [a] Value calculated at 120 min; [b] TOF_{max} = max value of *TOF* during photocatalysis; [c] Value obtained according to Equation S2.

Table S5. Ratios of absorbances (A) at 280 nm and 450 nm for each of the fractions of apoCB5:CoSalen 1:5 purified by SEC-MALS.

Multimer	Monomer	Dimer	Trimer	Tetramer	Larger
Ratio → / Sample↓	A_{280}/A_{450}	A_{280}/A_{450}	A_{280}/A_{450}	A_{280}/A_{450}	A_{280}/A_{450}
Expected	**10.5**	**10.5**	**10.5**	**10.5**	**10.5**
Before	12.1	11.6	11.3	11.2	12.0
Dark	11.5	10.5	10.5	10.5	10.8
0.5 min	9.5	9.4	9.4		9.4
120 min	6.0	5.9	5.8		5.7

Conditions: The before sample contains only *apo*CB5:CoSalen 1:5, the dark sample contains *apo*CB5:CoSalen 1:5, $[Ru(bpy)_3](ClO_4)_2$ and $Na_2S_2O_8$, the irradiated samples contain *apo*CB5:CoSalen 1:5, $[Ru(bpy)_3](ClO_4)_2$ and $Na_2S_2O_8$ and were irradiated with a 450 nm LED for respectively 0.5 min and 120 min. The "expected" ratios were determined based on UV-Vis data for a non-irradiated sample of *apo*CB5:CoSalen 1:5 in absence of $[Ru(bpy)_3](ClO_4)_2$ and $Na_2S_2O_8$.

6.4 Supplementary D: Supplementary figures

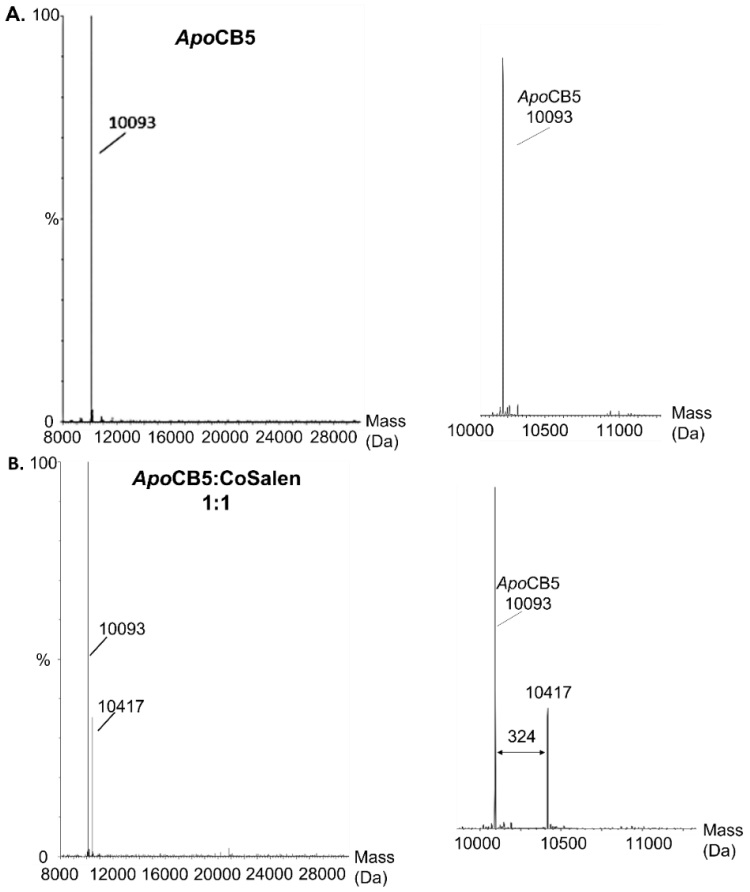

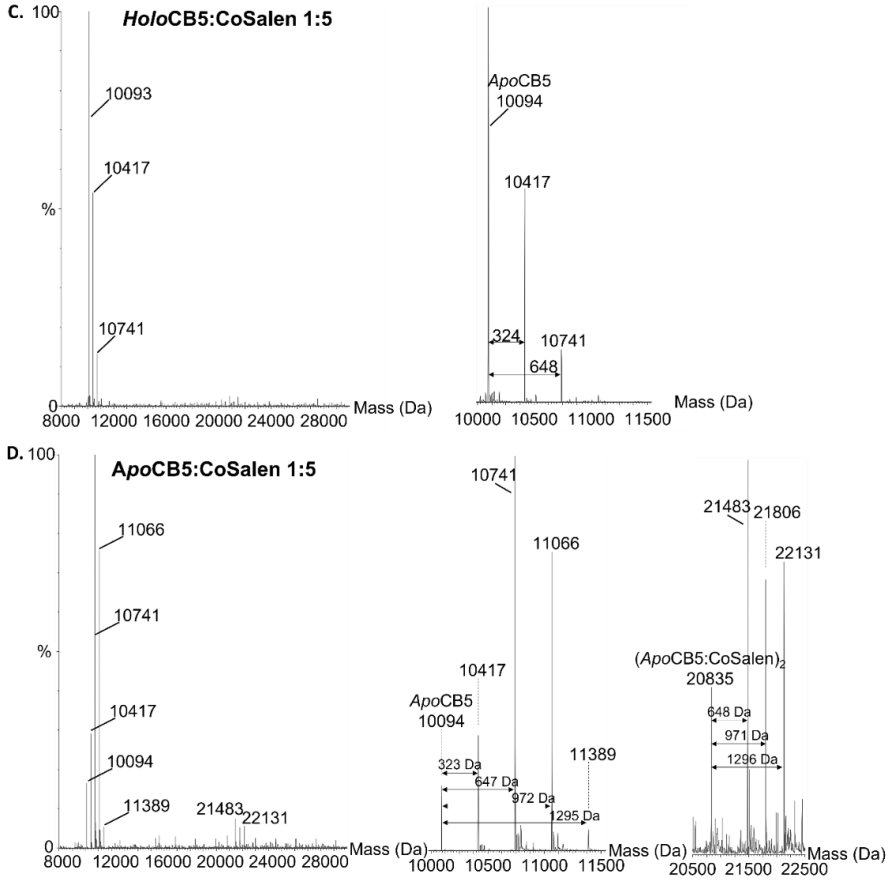

*Figure S3. Mass spectroscopy of the CB5 samples. In each case, a full spectrum is shown first, with on the left a zoom of any relevant regions. ApoCB5 (**A**), apoCB5:CoSalen 1:1 (**B**), holoCB5:CoSalen 1:5 (**C**), apoCB5:CoSalen 1:5 (**D**).*

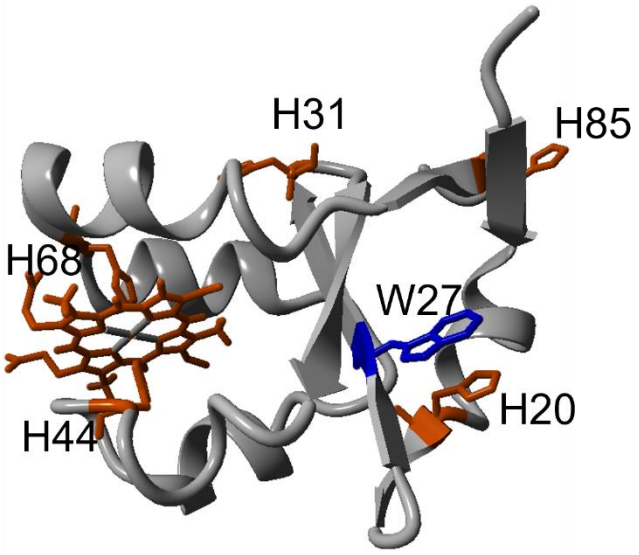

Figure S4. Homology model of cytochrome b_5 with all histidines (orange) and tryptophans (blue) shown explicitly (the homology model was prepared as detailed in supplementary B).

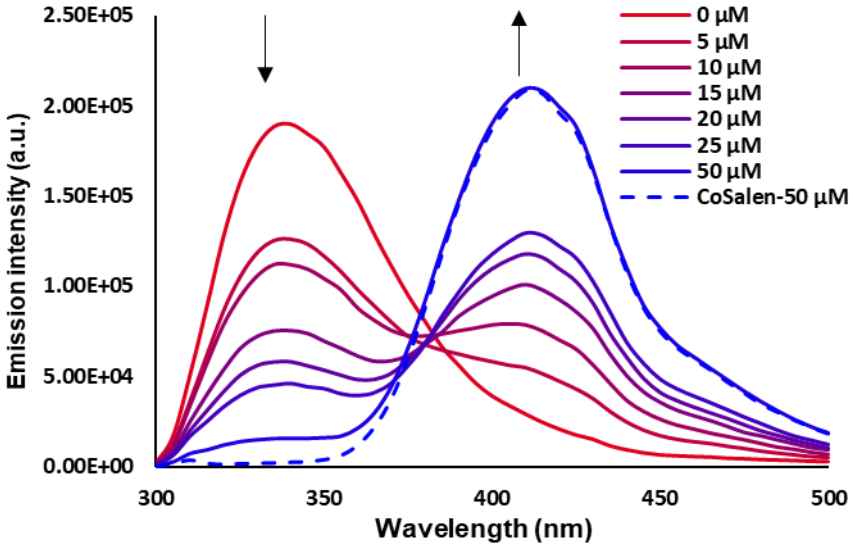

Figure S5. Emission spectra of a titration of apoCB5 with CoSalen in phosphate buffer pH 7.5. The excitation wavelength was 280 nm.

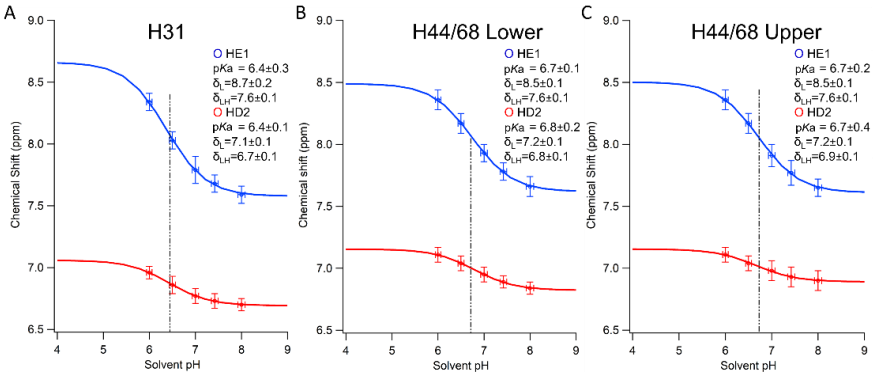

Figure S6. The pH dependence per histidine side chain of apoCB5 of the proton chemical shift as determined by large window HSQC NMR in the range pH 6.0-8.0. Data for H31 is shown in panel A, the more downfield (in the nitrogen dimension) of the two sets of peaks assigned to the binding pocket histidines (H44/H68) in panel B, the more upfield of the binding pocket histidines in panel C. In each dataset the data is fitted using Igor Pro version 6.37 from WaveMetrics (Oregon, USA) using the following equation: $\delta_{\mathrm{Obs}} = \frac{\delta_{\mathrm{L}} + \delta_{\mathrm{HL}} * 10^{\mathrm{pH - p}Ka}}{1 + 10^{\mathrm{pH - p}Ka}}$*, the resulting parameters are given in the top right corner in each panel. The pKa for each histidine is also indicated with a plain line. In each panel the NE2 HE1 peak chemical shift and trace are given in blue and the NE2 HD2 peak chemical shift and trace in red. The data points with their chemical shift error given by the full-width half of the maximum and a 1.0% error for the solvent pH are indicated in the figure.*

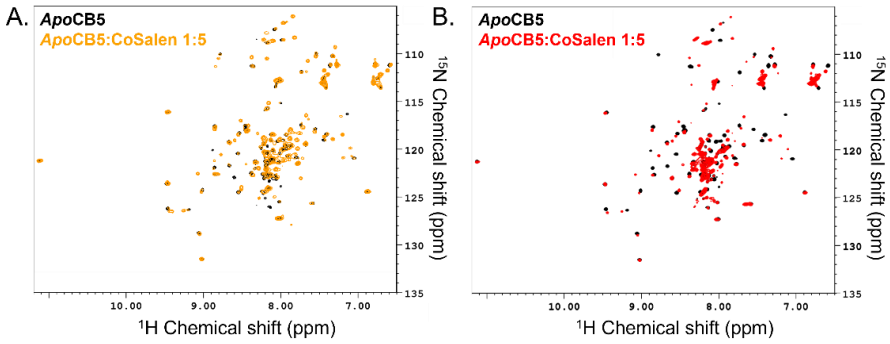

*Figure S7. HSQC NMR of apoCB5 (black), apoCB5:CoSalen 1:1 (**A**, orange), and apoCB5:CoSalen 1:5 (**B**, red).*

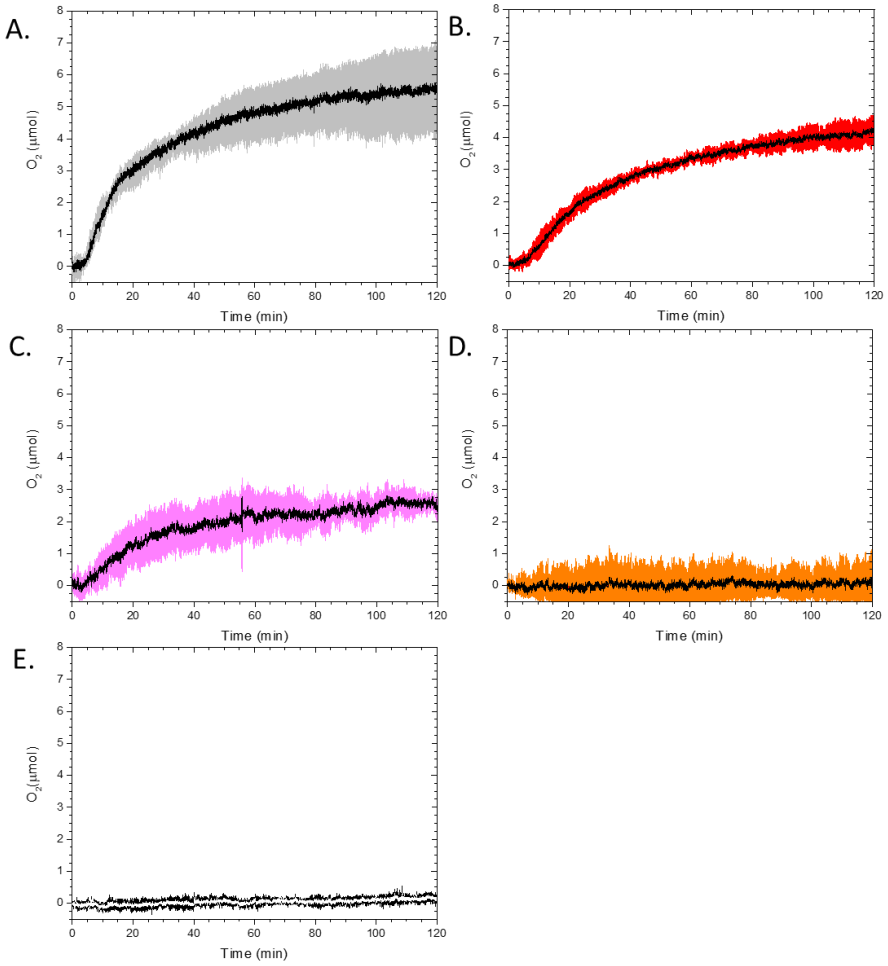

*Figure S8. Photoactivated water oxidation activity of CoSalen (**A**), apoCB5:CoSalen 1:5 (**B**), holoCB5:CoSalen 1:5 (**C**), apoCB5:CoSalen 1:1 (**D**), and apoCB5 (**E**) all with a CoSalen concentration of 50 µM (apoCB5 in **E** was 50 µM in CB5), in the presence of 0.3 mM $[Ru(bpy)_3](ClO_4)_2$ and 5 mM $Na_2S_2O_8$ upon irradiation with a 450 nm LED. The standard deviation is shown in colour surrounding the average trace in black (white in the case of apoCB5, E). Each trace is an average of at least 2 measurements.*

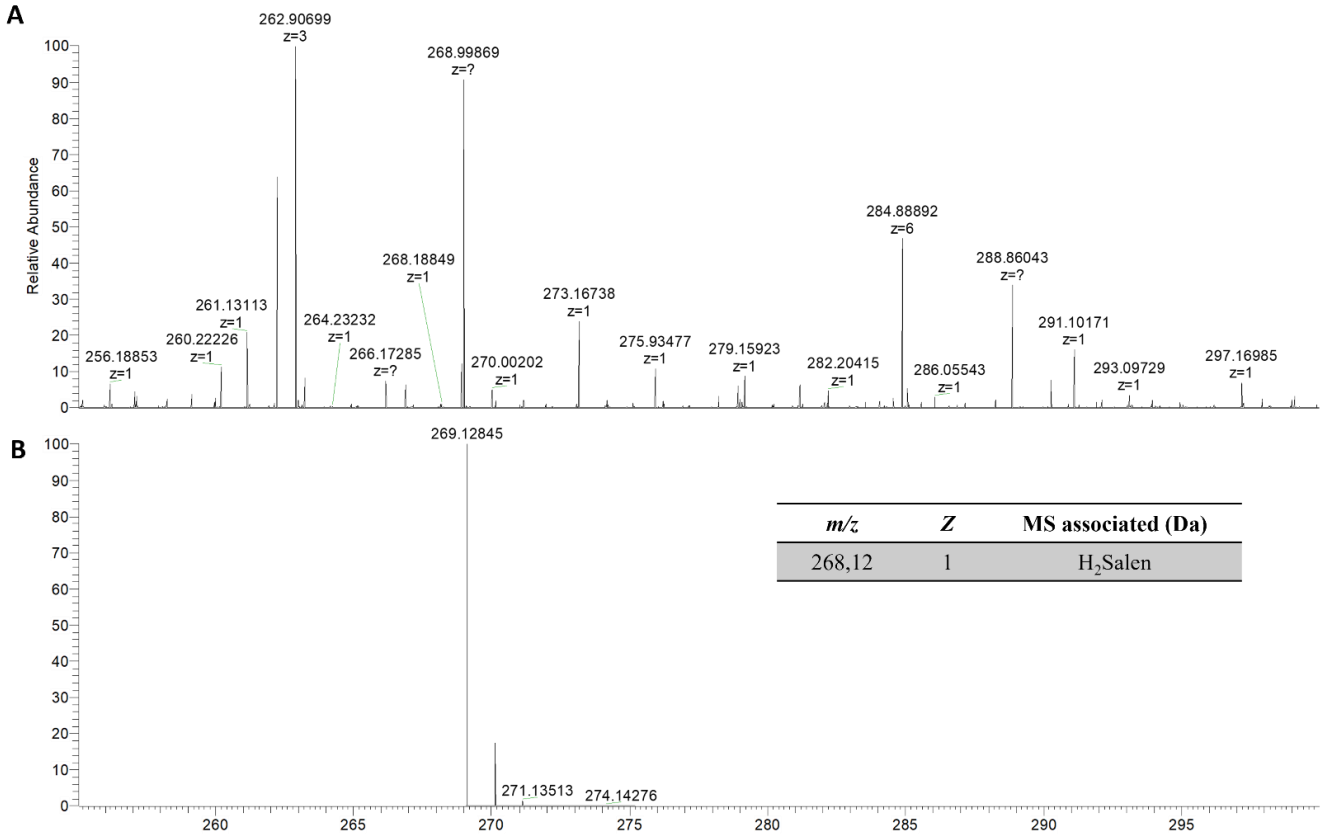

m/z	*Z*	MS associated (Da)
268,12	1	H_2Salen

*Figure S9. Deconvoluted HR-MS of apoCB5:CoSalen 1:5, [Ru(bpy)$_3$](ClO$_4$)$_2$ and $Na_2S_2O_8$ after photocatalysis, 120 min irradiation in phosphate buffer pH 7.5 80 mM. (**A**) Measured and (**B**) calculated for [M +H]*

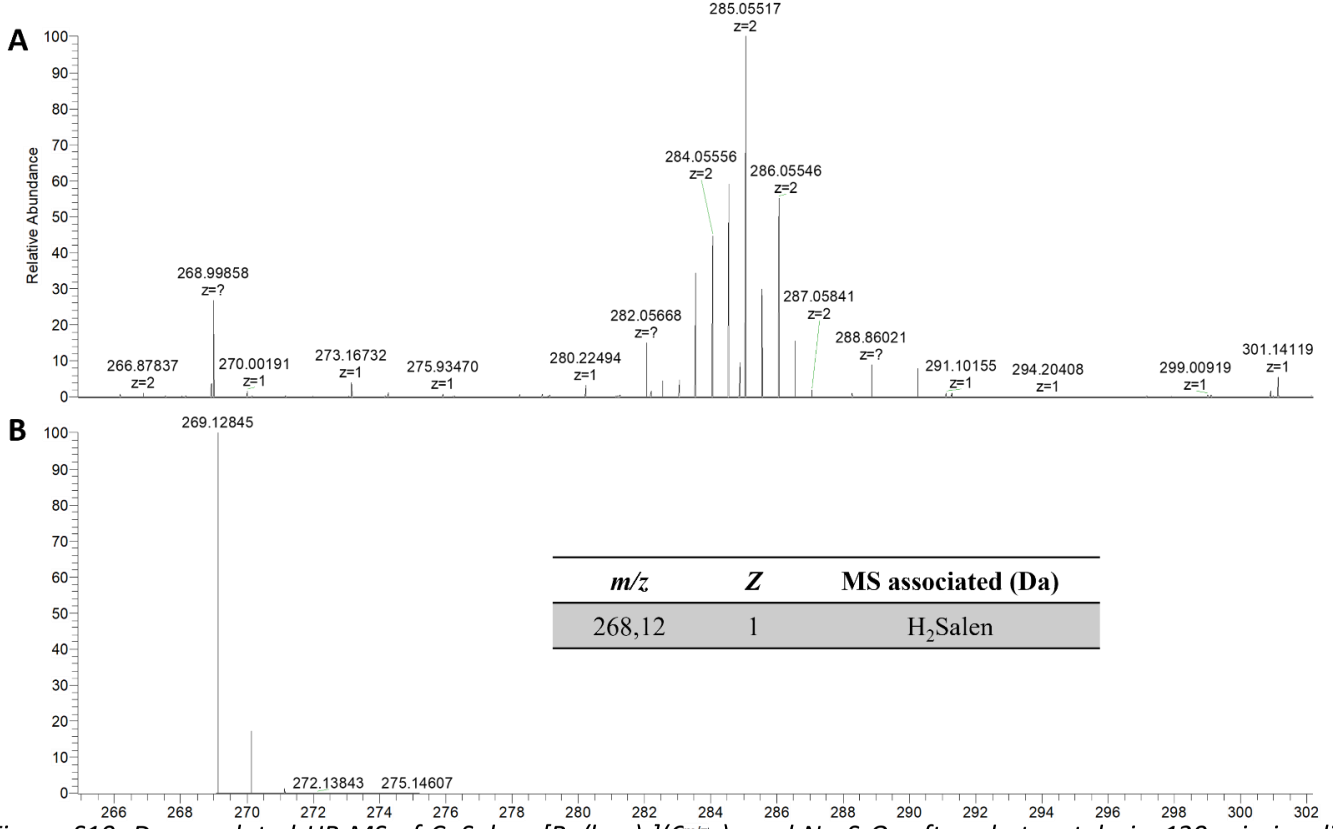

*Figure S10. Deconvoluted HR-MS of CoSalen, $[Ru(bpy)_3](ClO_4)_2$ and $Na_2S_2O_8$ after photocatalysis, 120 min irradiation in phosphate buffer pH 7.5 80 mM, 450 nm LED. (**A**) Measured and (**B**) calculated for [M +H]*

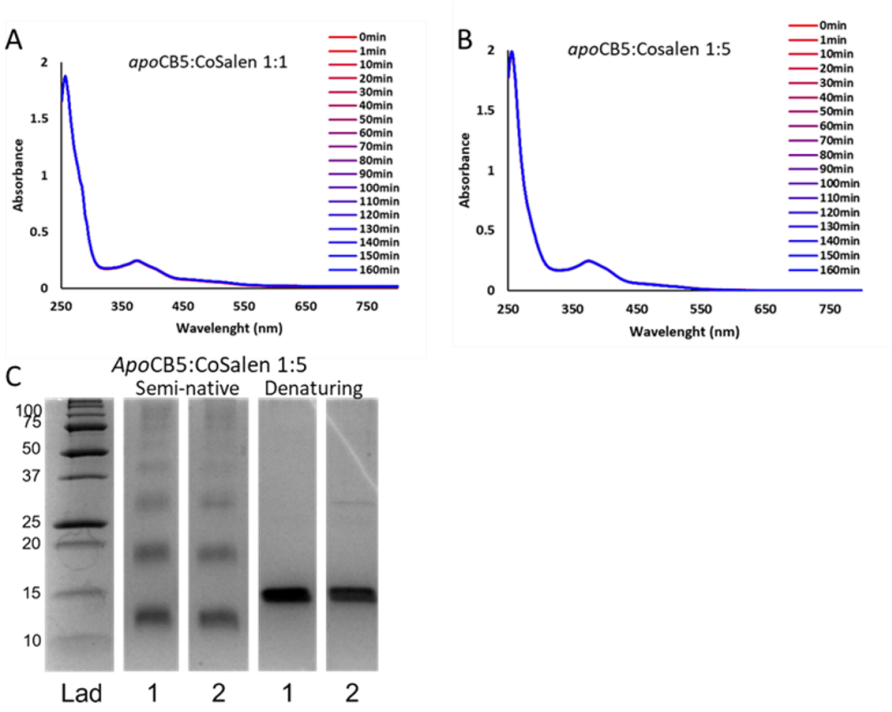

*Figure S11. UV-vis-spectra of apoCB5:CoSalen 1:1 (**A**) and apoCB5:CoSalen 1:5 (**B**). Spectra were recorded vs. time for 160 min under constant irradiation using a 450 nm LED light source. All samples were measured in 80 mM NaPi buffer pH 7.5 with a protein concentration of 50 µM. Red colour indicates t=0 min; blue colour indicates t=160 min, Semi-native (2nd and 3rd lane) and denaturing (4th and 5th lane) PAGE (**C**), visualized with coomassie, of apoCB5:CoSalen 1:5 before irradiation (lanes 1) and after irradiation (lanes 2) with the protein ladder in the left-most lane with molecular weight in kDa indicated on the left.*

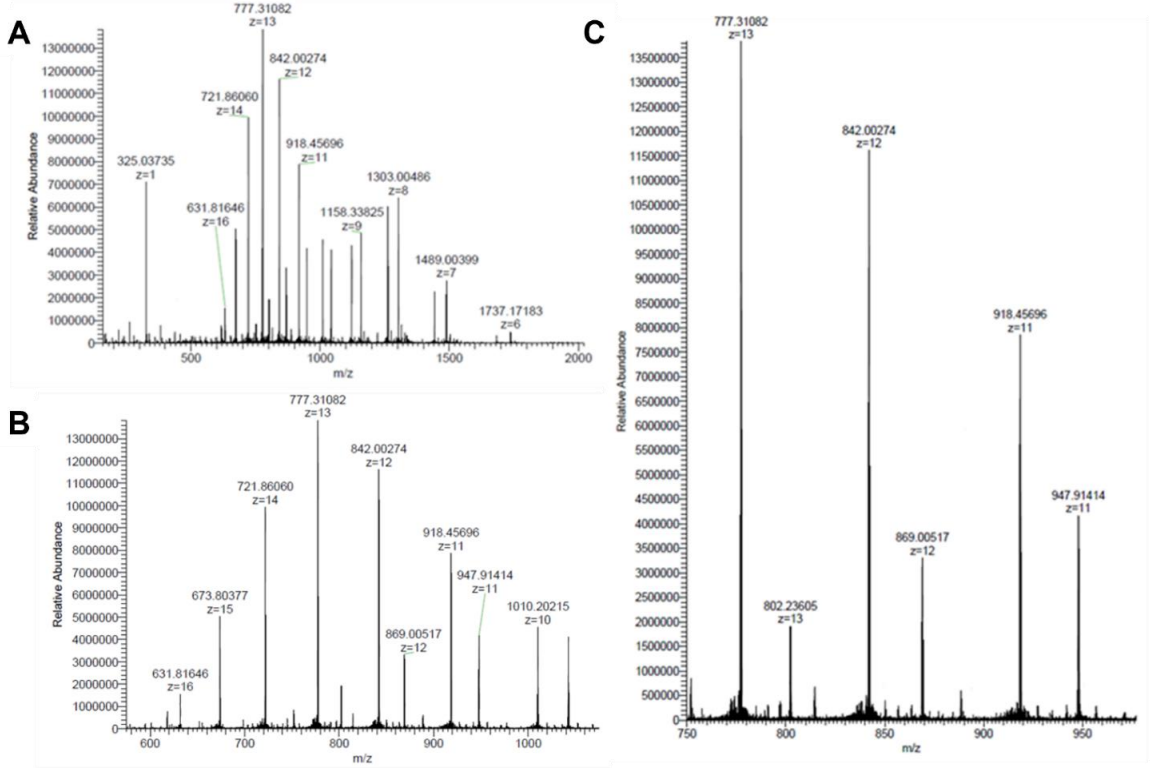

m/z	MS associated (Da)
325	CoSalen
631	*apo*CB5
673	*apo*CB5
722	*apo*CB5
777	*apo*CB5
842	*apo*CB5
918	*apo*CB5
1010	*apo*CB5
802	*apo*CB5:Cosalen 1:1
869	*apo*CB5:Cosalen 1:1
947	*apo*CB5:Cosalen 1:1
1158	*apo*CB5:Cosalen 1:1
1303	*apo*CB5:Cosalen 1:1
1489	*apo*CB5:Cosalen 1:1

*Figure S12. Deconvoluted HR-MS of apoCB5:CoSalen 1:1 after 160 min irradiation in phosphate buffer pH 7.5 80 mM, 450 nm LED. (**A**) from 0 to 2000 m/z; (**B**) from 600 to 1200 m/z; (**C**) from 750 to 980 m/z.*

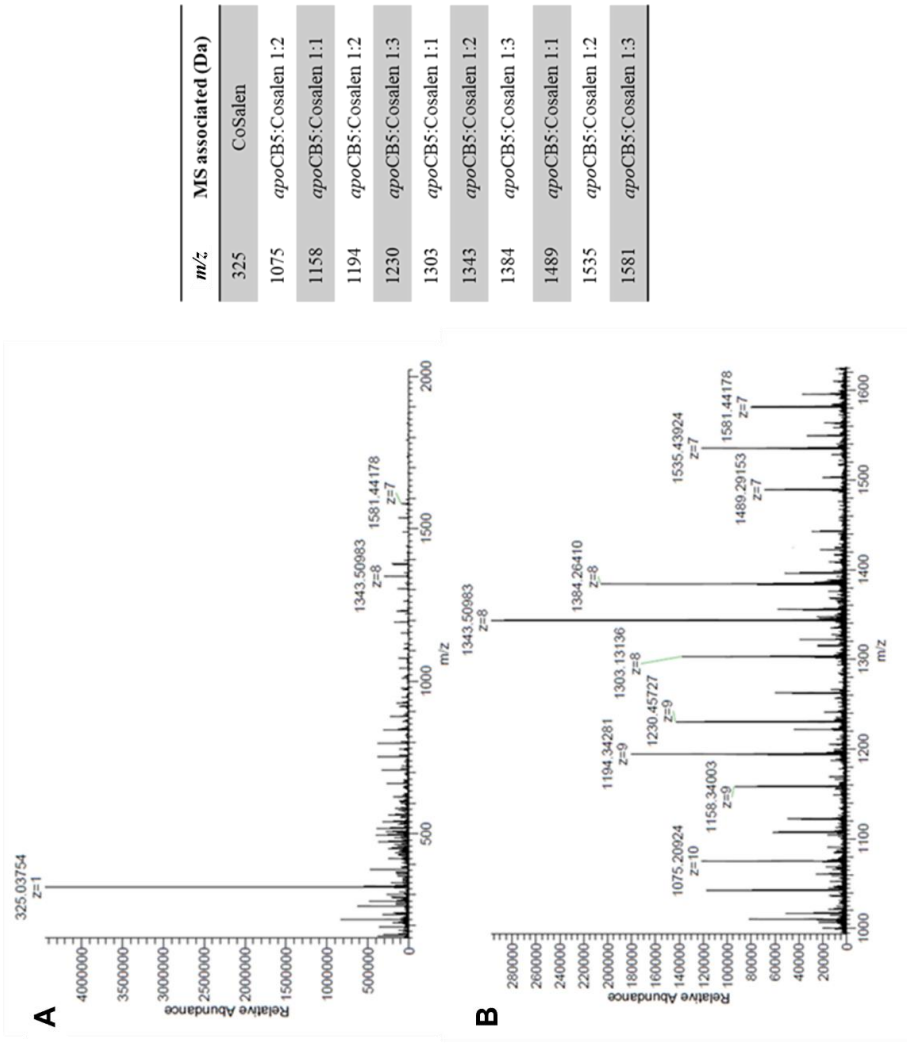

*Figure S13. Deconvoluted HR-MS apoCB5:CoSalen 1:5 after 160 min irradiation in phosphate buffer pH 7.5 80 mM, 450 nm LED. (**A**) from 0 to 2000 m/z; (**B**) from 1000 to 1600 m/z.*

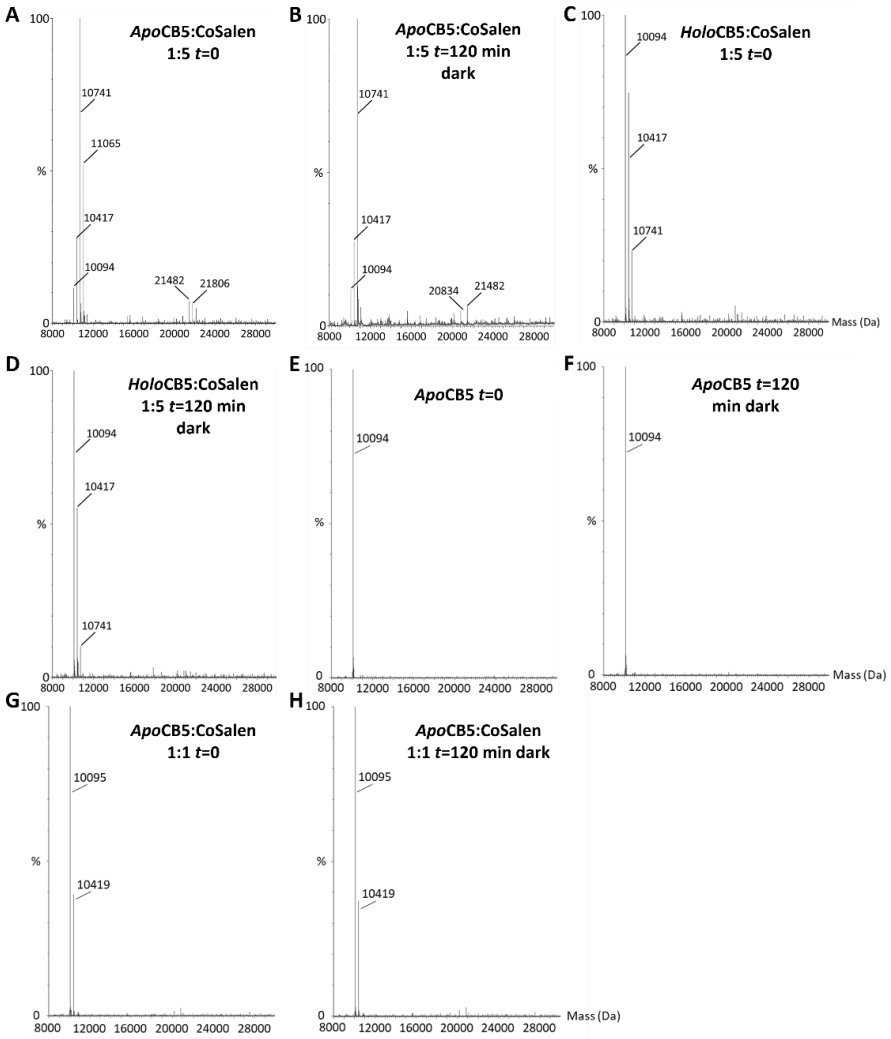

*Figure S14. Electrospray Ionization Mass Spectrometry (ESI-MS) of the following samples, each in 80 mM NaPi pH 7.5 and kept dark and at room temperature after the addition of $[Ru(bpy)_3](ClO_4)_2$ (0.3 mM) and $Na_2S_2O_8$ (5 mM), apoCB5:CoSalen 1:5 t= 0 min (**A**), apoCB5:CoSalen 1:5 t= 120 min (**B**), holoCB5:CoSalen 1:5 t=0 min (**C**), holoCB5:CoSalen 1:5 t= 120 min (**D**), apoCB5 t= 0 min (**E**), apoCB5 t= 120 min (**F**), apoCB5:CoSalen 1:1 t= 0 min (**G**), apoCB5:CoSalen 1:1 t= 120 min (**H**).*

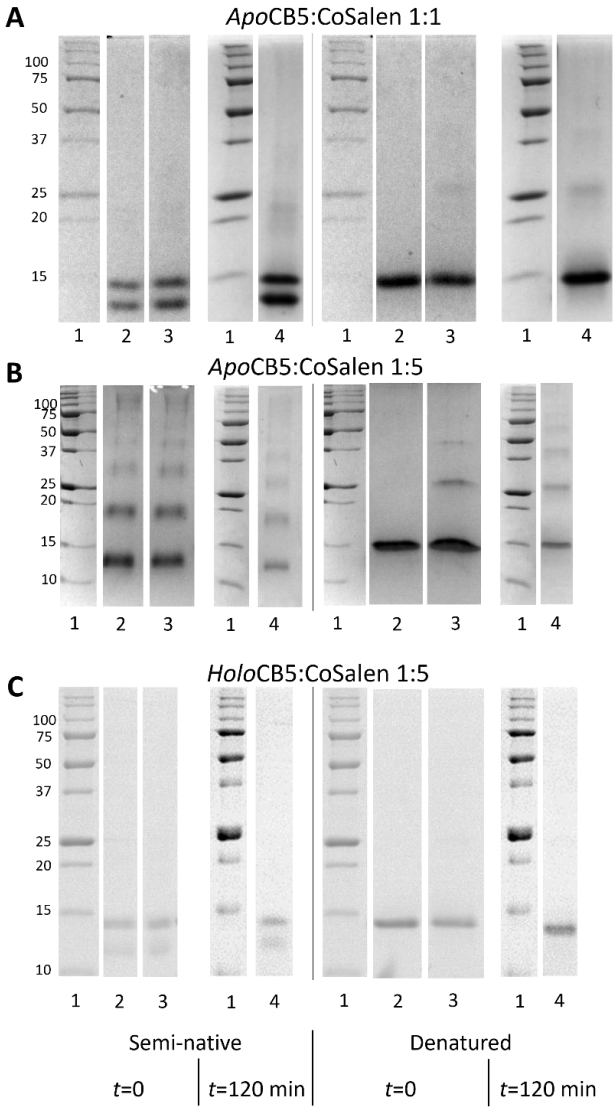

*Figure S15. Semi-native (**left**) and SDS- (**right**) PAGE of apoCB5:CoSalen 1:1 (**A**), apoCB5:CoSalen 1:5 (**B**), and holoCB5:CoSalen (**C**), each in 80 mM NaPi pH 7.5 and kept dark and at room temperature (visualized with coomassie): Lanes 1: protein ladder with molecular weight indicated left, lanes 2: protein only, lanes 3: protein directly after the addition of $[Ru(bpy)_3](ClO_4)_2$ (0.3 mM) and $Na_2S_2O_8$ (5 mM), lanes 4: protein + $[Ru(bpy)_3](ClO_4)_2$ (0.3 mM) + $Na_2S_2O_8$ (5 mM) after 120 min.*

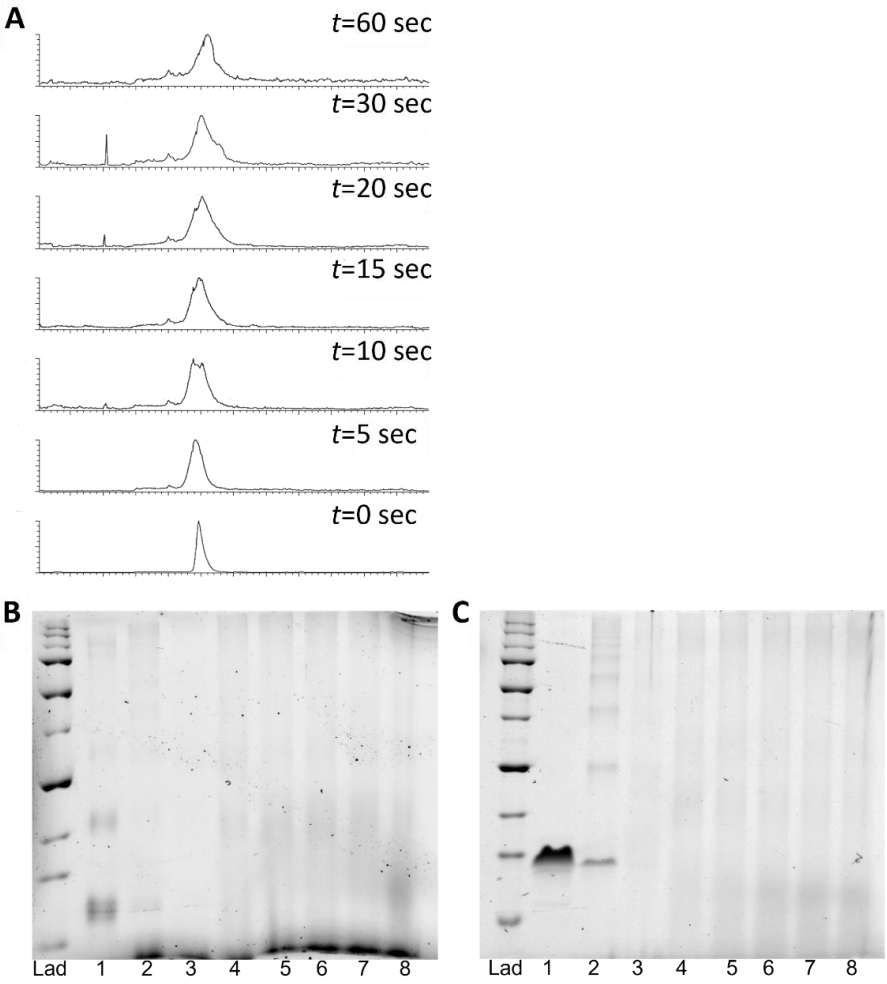

*Figure S16. Chromatograms of the C4 column run prior to mass spectrometry (**A**) of apoCB5:CoSalen 1:5 + 0.3 mM $[Ru(bpy)_3](ClO_4)_2$ + 5 mM $Na_2S_2O_8$ irradiated at 450 nm in the Clark setup for the time indicated in the figure. Semi-native (**B**) and denaturing (**C**) gel electrophoresis visualized with 2,2,2-trichloroethanol. Lane 1 contains apoCB5:CoSalen 1:5, in lanes 2-8 0.3 mM $[Ru(bpy)_3](ClO_4)_2$ and 5 mM $Na_2S_2O_8$ have been added and irradiation with a 450 nm LED in the Clark setup is performed for Lane 2: 0 s, Lane 3: 5 s, Lane 4: 30 s, Lane 5: 60 s, Lane 6: 90 s, lane 7: 120 s and lane 8: 150 s.*

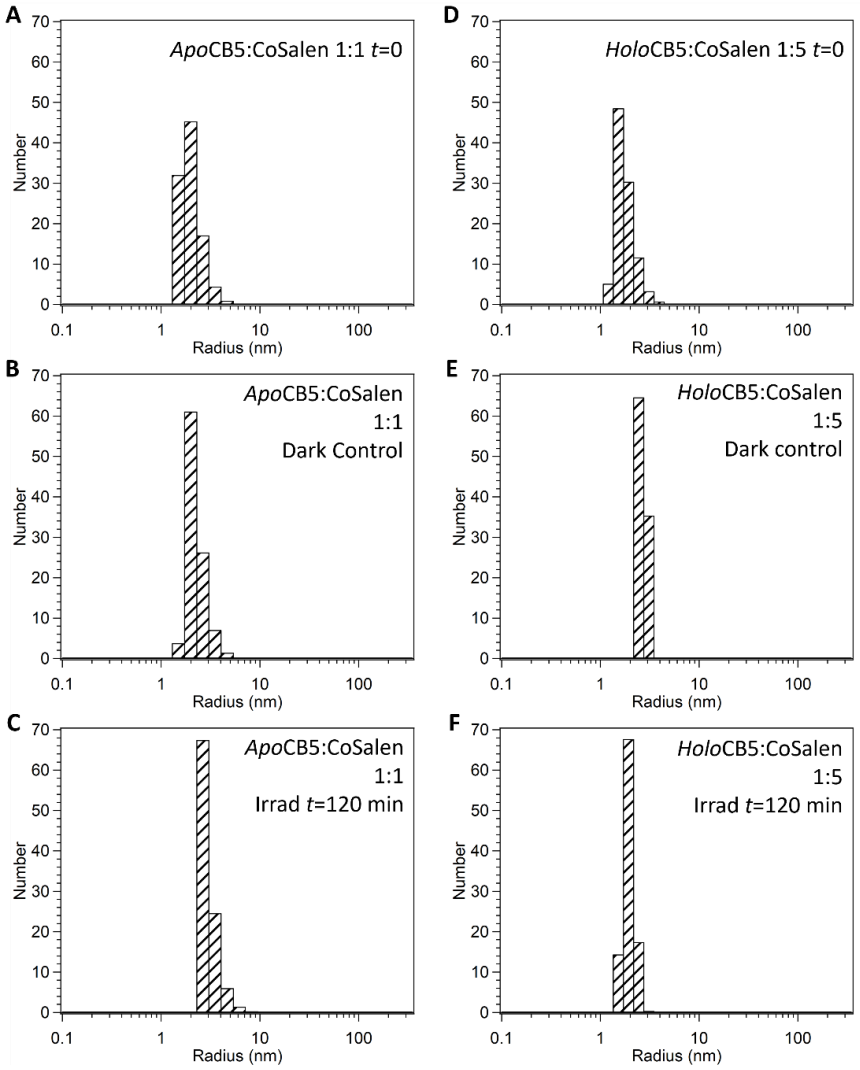

*Figure S17. Dynamic light scattering (DLS) analysis of apoCB5:CoSalen 1:1 and holoCB5:CoSalen 1:5 showing the percentage of the number of particles. All samples contain 50 µM CoSalen bound to CB5 in 80 mM NaPi pH 7.5. In the left panel, the following graphs can be observed: DLS of apoCB5:CoSalen 1:1 directly after the addition of 0.3 mM $[Ru(bpy)_3](ClO_4)_2$ and 5 mM $Na_2S_2O_8$ (**A**), apoCB5:CoSalen 1:1 + 0.3 mM $[Ru(bpy)_3](ClO_4)_2$ + 5 mM $Na_2S_2O_8$ after 120 min dark at room temperature (**B**) and apoCB5:CoSalen 1:1 + 0.3 mM $[Ru(bpy)_3](ClO_4)_2$ +5 mM $Na_2S_2O_8$ after 120 min irradiation at 450 nm at room*

*temperature (**C**). On the right DLS of holoCB5:CoSalen directly after addition of 0.3 mM $[Ru(bpy)_3](ClO_4)_2$ and 5 mM $Na_2S_2O_8$ (**D**), holoCB5:CoSalen + 0.3 mM $[Ru(bpy)_3](ClO_4)_2$ +5 mM $Na_2S_2O_8$ after 120 min dark at room temperature (**E**) and holoCB5:CoSalen + 0.3 mM $[Ru(bpy)_3](ClO_4)_2$ +5 mM $Na_2S_2O_8$ after 120 min irradiation with a 450 nm LED at room temperature (**F**).*

6.5 References

[1] S. Fu *et al.*, "A mononuclear cobalt complex with an organic ligand acting as a precatalyst for efficient visible light-driven water oxidation," *Chemical communications*, vol. 50, no. 17, pp. 2167–2169, 2014.

[2] S. Bienert *et al.*, "The SWISS-MODEL Repository—new features and functionality," *Nucleic acids research*, vol. 45, no. D1, pp. D313–D319, 2017.

[3] N. Guex, M. C. Peitsch, and T. Schwede, "Automated comparative protein structure modeling with SWISS-MODEL and Swiss-PdbViewer: A historical perspective," *Electrophoresis*, vol. 30, no. S1, pp. S162–S173, 2009.

[4] A. Waterhouse *et al.*, "SWISS-MODEL: homology modelling of protein structures and complexes," *Nucleic acids research*, vol. 46, no. W1, pp. W296–W303, 2018.

[5] G. Studer, C. Rempfer, A. M. Waterhouse, R. Gumienny, J. Haas, and T. Schwede, "QMEANDisCo—distance constraints applied on model quality estimation," *Bioinformatics*, vol. 36, no. 6, pp. 1765–1771, 2020.

[6] M. Bertoni, F. Kiefer, M. Biasini, L. Bordoli, and T. Schwede, "Modeling protein quaternary structure of homo-and hetero-oligomers beyond binary interactions by homology," *Scientific reports*, vol. 7, no. 1, p. 10480, 2017.

[7] C. J. Falzone, Y. Wang, B. C. Vu, N. L. Scott, S. Bhattacharya, and J. T. Lecomte, "Structural and dynamic perturbations induced by heme binding in cytochrome b 5," *Biochemistry*, vol. 40, no. 15, pp. 4879–4891, 2001.

[8] Y. Hirano, S. Kimura, and T. Tamada, "High-resolution crystal structures of the solubilized domain of porcine cytochrome b5," *Acta Crystallographica Section D: Biological Crystallography*, vol. 71, no. 7, pp. 1572–1581, 2015.

[9] S. Stoll and A. Schweiger, “EasySpin, a comprehensive software package for spectral simulation and analysis in EPR,” *Journal of magnetic resonance*, vol. 178, no. 1, pp. 42–55, 2006.

[10] C. Liu, D. van den Bos, B. den Hartog, D. van der Meij, A. Ramakrishnan, and S. Bonnet, “Ligand controls the activity of light-driven water oxidation catalyzed by nickel (II) porphyrin complexes in neutral homogeneous aqueous solutions,” *Angewandte Chemie International Edition*, vol. 60, no. 24, pp. 13463–13469, 2021.

[11] M. Laible and K. Boonrod, “Homemade site directed mutagenesis of whole plasmids,” *JoVE (Journal of Visualized Experiments)*, no. 27, p. e1135, 2009.

[12] F. Teale, “Cleavage of the haem-protein link by acid methylethylketone,” *Biochimica et biophysica acta*, vol. 35, p. 543, 1959.